JGR Atmospheres

RESEARCH ARTICLE

10.1029/2024JD042375

Microphysical and Kinematical Characteristics of Merged and Isolated Convective Cells Over the Complex Terrain of the Taipei Basin

Jyong-En Miao[1], **Ming-Jen Yang**[1], **Kristen L. Rasmussen**[2], **Michael M. Bell**[2], **Hung-Chi Kuo**[1], and **Ting-Yu Cha**[3]

[1]Department of Atmospheric Sciences, National Taiwan University, Taipei, Taiwan, [2]Department of Atmospheric Science, Colorado State University, Fort Collins, CO, USA, [3]National Center for Atmospheric Research, Boulder, CO, USA

Key Points:

- Multiple convective cell mergers favored by terrain-induced circulation led to intense updrafts and extreme rainfall over Taipei Basin
- Merged convective cells showed stronger updrafts, more graupel, and broader enhanced ZDR regions (>1 dB) than isolated cells
- A wide (>8 km) enhanced ZDR region at 5.5 km altitude formed during cell merger and was followed by intense updrafts and rainfall

Supporting Information:

Supporting Information may be found in the online version of this article.

Correspondence to:

M.-J. Yang,
mingjen@as.ntu.edu.tw

Citation:

Miao, J.-E., Yang, M.-J., Rasmussen, K. L., Bell, M. M., Kuo, H.-C., & Cha, T.-Y. (2025). Microphysical and kinematical characteristics of merged and isolated convective cells over the complex terrain of the Taipei Basin. *Journal of Geophysical Research: Atmospheres*, *130*, e2024JD042375. https://doi.org/10.1029/2024JD042375

Received 2 SEP 2024
Accepted 14 JUL 2025

Author Contributions:

Conceptualization: Ming-Jen Yang, Kristen L. Rasmussen
Data curation: Ting-Yu Cha
Formal analysis: Jyong-En Miao
Funding acquisition: Ming-Jen Yang
Investigation: Jyong-En Miao, Ming-Jen Yang, Kristen L. Rasmussen, Michael M. Bell, Hung-Chi Kuo
Methodology: Jyong-En Miao, Ming-Jen Yang
Project administration: Ming-Jen Yang
Resources: Ming-Jen Yang, Hung-Chi Kuo

Abstract

This study investigates the microphysical and kinematic characteristics in extreme afternoon thunderstorm rainfall during Taiwan-Area Heavy rain Observation and Prediction Experiment/Prediction of Rainfall Extremes Campaign In the Pacific IOP 2. The high-quality S-Pol radar observations and multi-Doppler winds provided valuable information about the convective organization over complex terrain. There were two episodes of heavy rainfall in this event. Episode 1 (1200–1400 LST, Local Standard Time) featured multiple cell merger (MCM) favored by terrain-induced circulation. Around the time of MCM, the enhanced ZDR region (>1 dB) broadened horizontally to ∼8 km in width at 5.5 km above mean sea level (AMSL). Afterward, maximum vertical velocity increased dramatically to ∼20 m s^{-1} and graupel reached up to 12 km AMSL. In contrast, Episode 2 (1500–1700 LST) exhibited isolated cells with weak updrafts (<10 m s^{-1}) and more snow aloft. The merged ZDR columns coincided with MCM occurrence, preceding peaks in both vertical velocity and rainfall intensity. Building on emerging research investigating the relationship between ZDR column size and severe weather in the US, this study suggests that wide merged ZDR columns may be relevant to severe storms over complex terrain in Taiwan, highlighting their potential utility as indicators of storm intensification.

Plain Language Summary

Thunderstorms can produce extreme rainfall, especially over mountainous areas, leading to severe weather events such as flash floods. Understanding how these storms develop and what makes them so intense is crucial for improving weather forecasts. This study analyzed thunderstorms over the complex terrain of the Taipei Basin using advanced radar observations that have been previously unavailable in northern Taiwan. These storms were observed during an international field campaign in 2022 and were notable for the extreme rainfall over the mountainous region. We specifically looked at how the storms' characteristics, such as their updrafts and precipitation patterns, evolved over time. We found that during the most intense phase of the storm, multiple convective cells merged together, leading to intense updrafts and heavy rainfall. By comparing different stages of the storm, our findings indicate that the widening of enhanced ZDR region may offer useful clues about the storm intensification. These results can help improve how we monitor and forecast dangerous storms in Taiwan's mountainous regions.

1. Introduction

The Taipei Basin, the most populous and economically significant region in Taiwan, experiences a strong influence from afternoon thunderstorms (ATSs) during the warm season (Chen et al., 2007). The Taipei metropolitan area often faces severe property damage and traffic hazards due to flash flooding and lightning associated with intense ATSs. Additionally, ATSs in Taiwan pose risks to people visiting mountainous areas and streams during the summer. A sudden rise in water level can result in incidents such as being stranded or swept away by fast currents, leading to the loss of human lives. Despite their significant impacts, forecasting ATSs remains challenging for meteorologists (Yang et al., 2024), in part due to our limited understanding of their underlying physical mechanisms and multiscale nature.

Predicting thunderstorms over mountainous regions is challenging due to the multiscale interactions of various atmospheric processes, including solar heating, thermally driven airflow, cloud microphysics, cold pools, and topographic effects (Du et al., 2020; Houze, 2012; Huang et al., 2019; Li et al., 2021; Morrison et al., 2020; Xu et al., 2012). Nonlinear interactions between convective cells may increase the intensity of thunderstorms and the amount of rainfall (Glenn & Krueger, 2017; Tao & Simpson, 1989; Westcott, 1984). Additionally, the terrain of

Software: Jyong-En Miao, Michael M. Bell, Ting-Yu Cha
Supervision: Ming-Jen Yang, Kristen L. Rasmussen
Validation: Jyong-En Miao
Visualization: Michael M. Bell
Writing – original draft: Jyong-En Miao
Writing – review & editing: Ming-Jen Yang, Kristen L. Rasmussen, Michael M. Bell, Hung-Chi Kuo

Taiwan modifies the flow patterns and environmental characteristics, leading to variations in the location and intensity of precipitation (Cornejo et al., 2024; Miao and Yang, 2020, 2022). For example, Miao and Yang (2020) demonstrated that coastal terrain enhances sea-breeze circulation through the channel effect, transporting more moisture into the Taipei Basin, which contributes to increased precipitation over the region. This complexity adds to the challenge of accurately predicting convection initiation, propagation, and intensification. Gaining a deeper understanding of the underlying physical mechanisms responsible for ATSs is essential for enhancing forecasting capabilities and implementing effective measures for disaster prevention.

Polarimetric radars provide invaluable insights into the microphysics and kinematics of updrafts in convective systems. For instance, differential reflectivity (ZDR) measures the difference between horizontally and vertically polarized radar reflectivity factors on a logarithmic scale, providing information about the shapes of particles, especially when these particles are small relative to the radar wavelength. One key polarimetric feature is the ZDR column, a ZDR-enhanced region extending above the environmental 0°C isotherm in the updraft area of severe storms (Kumjian et al., 2014; Loney et al., 2002). It may contain low concentrations of large supercooled raindrops, ice crystals, graupel, and hail undergoing wet growth (Bringi et al., 1997; Illingworth et al., 1987; Kumjian et al., 2014). The ZDR column in midlatitude thunderstorms can extend 3 km or more above the environmental 0°C level (Kumjian et al., 2014; Kuster et al., 2019; Tuttle et al., 1989). However, in subtropical storms, ZDR columns typically develop to heights of 1–2 km above the freezing level (Jung & Jou, 2023, hereafter JJ23; Yu et al., 2022). Snyder et al. (2015) developed an algorithm that can identify and quantify ZDR columns in operational weather radar data, which could help evaluate convective storm evolution. Recent studies (e.g., French & Kingfield, 2021; Kuster et al., 2019) have explored ZDR column area for its potential in operational storm predictions in the US, specifically for estimating storm intensity and nowcasting severe weather.

Another strength of polarimetric radars is the capability to detect changes in particle size, shape, orientation, and phase composition during various microphysical processes. Consequently, each microphysical process may leave a distinct polarimetric fingerprint that can be used to identify the process (Kumjian et al., 2022). For instance, Kumjian and Ryzhkov (2012) proposed a framework to infer the dominant precipitation processes by examining the vertical gradient of radar reflectivity (ZH) and ZDR within the warm cloud layer. In the tropical DYNAMO/ARM-AMIE data set of radar observations, most of the convection cases reveal fingerprints for coalescence and evaporation while many stratiform cases reveal fingerprints for breakup, coalescence and evaporation (Kumjian & Prat, 2014).

The "Taiwan-Area Heavy rain Observation and Prediction Experiment" (TAHOPE, 2022) field campaign was conducted from 25 May to 10 August 2022 to study the key ingredients and processes leading to extreme rainfall over complex terrain in Taiwan. Taiwan-Area Heavy rain Observation and Prediction Experiment (TAHOPE) is an international field campaign in collaboration with the Prediction of Rainfall Extremes Campaign In the Pacific (PRECIP, 2022) from the US, and the Tropical cyclones-Pacific Asian Research Campaign for Improvement of Intensity estimations/forecasts (T-PARCII, 2022) from Japan to have synergistic research observations. One of the primary scientific objectives of TAHOPE was to study the initiation, development and cloud-microphysical processes of ATSs that produce extreme precipitation over complex terrain. Complementary objectives from the PRECIP field campaign to study the key ingredients leading to heavy rainfall in a moisture-rich environment using an ingredients-based framework (Doswell et al., 1996) led to the deployment of the National Center for Atmospheric Research (NCAR) S-band dual-polarization Doppler radar (S-Pol) in Hsinchu, Taiwan. These observations provide high-quality plan position indicator (PPI; horizontal scanning strategy) and range height indicator (RHI; vertical cross sections) scans of polarimetric observations in deep convection.

The convective cell merger process occurs when two or more convective cells merge and form a larger and more intense storm (Carey & Rutledge, 2000; Glenn & Krueger, 2017; Moseley et al., 2016; Tao & Simpson, 1989). This process played an important role in the development of ATSs over the Taipei Basin (Jou et al., 2016; Miao & Yang, 2018) and also occurred in TAHOPE/PRECIP IOP 2 (31 May 2022). JJ23 suggested that decreased ZDR and increased specific differential phase (KDP) near the 0°C level after the merging indicated the increasing graupel concentration. The abundance of melted graupel enhanced ZDR and KDP below the 0°C level, which was related to the subsequent heavy rain. Based on a WRF simulation with the horizontal grid size nested down to 0.5 km, Miao and Yang (2018) proposed two physical mechanisms of cell mergers, highlighting the role of environmental winds, cold pools, and topography in the organization of thunderstorms. The first type of merger was the "rear-end collision" associated with different cell propagation speeds. After the convective cells reached the mature stage, the second type of merger was the "head-on collision" between the precipitation-induced outflows in the opposite direction (Tao & Simpson, 1989).

Although polarimetric radars have significantly advanced our understanding of microphysical processes in convective storms, detailed case studies focusing on thunderstorms in northern Taiwan remain limited (e.g., JJ23). Most prior research has been conducted in the US, particularly over the Great Plains, where environmental conditions and orographic characteristics differ substantially from those in Taiwan (e.g., Bodine & Rasmussen, 2017; Klaus et al., 2023; Kumjian & Ryzhkov, 2008; Picca & Ryzhkov, 2012; Segall et al., 2022; Tam et al., 2022; Van Den Broeke, 2017; Van Den Broeke, 2020; Wilson & Van Den Broeke, 2021). Moreover, previous studies on ATSs over the Taipei Basin (e.g., JJ23) used reconstructed RHIs to identify ZDR columns and other polarimetric features. However, the time difference between radar scans and spatial interpolation errors may significantly impact the pseudo-RHI results (Snyder et al., 2015), limiting the interpretation.

High-quality RHIs from the S-Pol radar can provide detailed insights into the microphysical and kinematical characteristics of deep convection that were unavailable for previous studies in northern Taiwan. In addition, we used the Spline Analysis at Mesoscale Utilizing Radar and Aircraft Instrumentation (SAMURAI-TERRAIN; Bell et al., 2012; Cha & Bell, 2023) software, a three-dimensional variational analysis method that can retrieve multi-Doppler winds over complex terrain. We investigate the microphysics and kinematics of the severe ATS in TAHOPE/PRECIP IOP 2 utilizing a unique combination of S-Pol observations and 3D winds retrieved by SAMURAI-TERRAIN. This is the first time this novel radar technique has been used to observe convective-scale processes in northern Taiwan. The primary objective of this study is to compare the microphysical and kinematic characteristics of merged and isolated convective cells, and to identify the key physical processes leading to the extreme orographic rainfall in ATSs. In addition, we investigate how updraft strength relates to observed ZDR column characteristics. By analyzing these advanced radar observations, we aim to gain new insights into the microphysical and kinematic characteristics of ATSs producing heavy rainfall over the mountainous region.

Section 2 details our data sources and the tracking algorithm. In Section 3, we analyze the pre-storm synoptic environment and storm evolution. The main results are presented in Section 4. Section 5 provides the discussions and conclusions.

2. Data and Methodology

2.1. Polarimetric Measurements From S-Pol

We utilized the level-II polarimetric products from the NCAR S-Pol radar (NCAR/EOL S-Pol Team, 2023) to examine polarimetric radar signatures in the ATSs on 31 May 2022, which was IOP 2 of TAHOPE/PRECIP. The S-Pol scanning strategy alternated between the PPI and RHI modes every 12 min. To ensure unbiased RHI sampling, the RHI mode employed a combination of fixed and user-defined azimuth angles. The fixed azimuth angles provided a statistically representative data set of convective structures, whereas the user-defined azimuth angles were adjusted in real time to target active convection regions. S-Pol plays a vital role in minimizing errors caused by attenuation and hail contamination (Chang et al., 2015). Most importantly, the S-Pol polarimetric RHI scans, which provide invaluable insights into the microphysical features of precipitation systems, have previously been unavailable for observational studies on the ATSs in northern Taiwan.

The Python ARM Radar Toolkit (Py-ART; Helmus & Collis, 2016) was used to interpolate PPI scans onto a Cartesian grid with a horizontal grid spacing of 1 km and a vertical grid spacing of 0.5 km. The primary radar parameters analyzed in this study were ZH, ZDR, and KDP. The quality control procedure removed radar gates with correlation coefficient (ρ_{HV}) < 0.8 or ZH < 0 dBZ to eliminate the non-hydrometeor signals. The particle identification (PID) provides the most likely particle type at every gate within the three-dimensional scan. This categorization is achieved using a fuzzy logic algorithm (Vivekanandan et al., 1999), which quantifies the probability of various particle types based on different polarimetric variable ranges. This study used the RadxPid algorithm within the Lidar Radar Open Software Environment (LROSE; DeHart et al., 2024) to perform PID, enabling robust hydrometeor classification.

2.2. Kinematic Field Retrieval From SAMURAI-TERRAIN

Multi-Doppler analyses were generated using the SAMURAI-TERRAIN software (Bell et al., 2012; Cha & Bell, 2023; Foerster & Bell, 2017), a component of the LROSE. SAMURAI-TERRAIN employs a three-

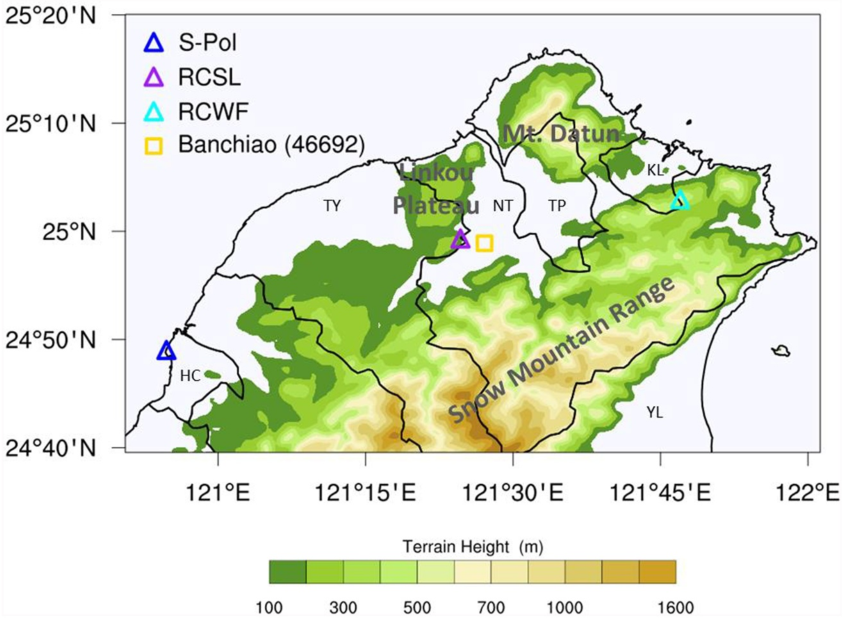

Figure 1. Northern Taiwan domain with terrain elevations plotted (colored; in units of meter). The primary instruments including S-Pol, RCWF, and RCSL radars are indicated. The location of the Banchiao sounding station (46692) is also labeled. The main cities on the map are Taipei (TP), New Taipei (NT), Keelung (KL), Taoyuan (TY), Hsinchu (HC), and Yilan (YL).

dimensional variational data assimilation technique, integrating radar observations and cubic b-spline basis functions to produce the most probable atmospheric state by minimizing a cost function. In this process, SAMURAI-TERRAIN calculates the three-dimensional wind field, incorporating mass continuity as a numerical constraint. Moreover, the impermeability and topographic forcing boundary conditions are implemented at the terrain height. The outcome is a 3D cubic spline representation of the wind field. The multi-Doppler winds were synthesized with a horizontal spline nodal spacing of 1 km and a vertical nodal spacing of 0.5 km. Gaussian filters with a $4\Delta x$ length in the horizontal plane and $2\Delta x$ length in the vertical direction were applied. This nodal spacing and filter length led to a minimum resolved scale of approximately 4 km horizontally. Further details on SAMURAI-TERRAIN can be found in Cha and Bell (2023).

This study utilizes RHI data from S-Pol radar and PPI data from RCWF and RCSL radars to perform wind retrieval (see the radar locations in Figure 1). RCWF is a WSR-88D dual-polarization radar operating in PPI mode, completing a full volume scan approximately every 6 min. RCSL is a METEOR 1700C C-band dual-polarization radar, also operating in PPI mode, with a volume scan interval of approximately 7 min. Further details on these radars can be found in Chang et al. (2021).

Before the wind retrieval process, the PPI data of RCWF and RCSL radars was quality-controlled using the Py-ART software. Additionally, the 78° and 83° RHI data of S-Pol radar are also quality-controlled and used in the wind retrieval to obtain better coverage of the wind analysis in deep convection. The 78° azimuth was selected to capture cell mergers in Episode 1, allowing detailed analysis of storm interactions, whereas the 83° azimuth targeted convection farther south in Episode 2. The time difference between the PPI scans from RCWF and RCSL and the RHI scans from S-Pol was less than 5 min. Utilizing data from PPI and RHI, the multi-Doppler analysis offered comprehensive 3D winds and further aided in analyzing the interaction between convective cells over complex terrain.

2.3. Tracking Algorithm for ZDR Columns

Detecting ZDR columns is complicated by the relatively limited mid-tropospheric resolution and coverage inherent in the scanning strategies of many operational weather radars (Snyder et al., 2015). Scanning in elevation (i.e., RHIs) helps eliminate spurious tilting caused by data collection delays and enables more accurate quantification of ZDR columns. Thus, we employed "tobac" (Heikenfeld et al., 2019), a recently developed framework designed for the tracking and analysis of individual features in various data sources, on the RHI data from S-Pol.

Using the Python package tobac, ZDR columns were identified in each RHI scan in the gridded field of ZDR. The tracking library allows for smoothing the input field using a Gaussian filter. After testing different smoothing options, we set the Gaussian filter to 1, which results in minimal smoothing of the ZDR field and keeps the details of the ZDR column structure in the original data. To detect ZDR columns, we adopted the ZDR threshold of 1 dB used in previous studies (Kuster et al., 2019; Snyder et al., 2015). The minimum number (15) of contiguous pixels for the feature to be detected is set to avoid extraneous points to be detected as erroneous features because the focus of this paper is on ZDR columns associated with the updrafts in deep convection. A ZDR column feature is hence defined as a contiguous area with ZDR $>$ 1 dB extending $\geq$5 km above mean sea level (AMSL).

2.4. Measurement of ZDR Column Width

Previous studies (e.g., French & Kingfield, 2021; Kuster et al., 2019) have analyzed updraft area proxies and found a positive correlation between ZDR column area and severe weather in the US, including large hail, damaging winds, and tornadoes. In this study, we utilize high-quality RHI scans to determine ZDR column width, rather than ZDR column area. Given that updraft width and area are related, this study directly measures proxies for updraft width. We focus on the width of the enhanced ZDR region ($>$1 dB) at 5.5 km AMSL, which is approximately 0.5 km above the environmental 0°C level based on the sounding data from this case and also consistent with the May–June climatology in northern Taiwan (Lee et al., 2019). This analysis height was selected to reduce potential contamination near the melting layer (French & Kingfield, 2021; Kuster et al., 2019; Van Den Broeke, 2017) while ensuring a sufficient sample size. The calculated width is defined as the maximum horizontal extent of enhanced ZDR values ($>$1 dB) at 5.5 km AMSL, representing their full coverage at that level.

3. Case Overview

The TAHOPE/PRECIP IOP 2 was chosen because it presented a unique opportunity to study ATSs producing extreme rainfall over complex terrain. The planning of TAHOPE/PRECIP IOP 2 anticipated heavy rainfall over the entire Taipei Basin, including both the basin plain and mountainous regions. However, the event resulted in heavy rainfall occurring predominantly over the mountainous areas, with significantly less precipitation observed in the basin plain. Additionally, operational model forecasts performed poorly for this extreme rainfall event. This case represents a unique opportunity to improve our understanding of the physical mechanisms leading to extreme orographic rainfall and to explore the limitations of current forecasting models. This section examines the synoptic conditions and storm evolution for this terrain-confined ATS event.

3.1. Synoptic Environment

On 31 May 2022 at 08 LST (00 UTC), a stationary frontal system was located over the northern ocean of Taiwan (Figure 2a). Synoptic-scale weather maps indicate prevailing southwesterly winds at 850–500 hPa near Taiwan (Figures 2b and 2c). The ridge associated with the subtropical high extended over the Bashi Channel and the South China Sea. The 200-hPa weather map reveals a diffluent upper-level wind field near Taiwan, which is conducive to upper-level divergence (Figure 2d).

The sounding at the Banchiao station (Figure 3a) indicated weak convective instability for the thermodynamic conditions at 0800 LST. Although the moisture was abundant at the low and middle levels, the near-surface inversion impeded the ascent of surface air parcels and led to an insignificant surface-based CAPE value (near 0 J kg^{-1}) in the morning. Weak winds prevailed in the Taipei Basin within the boundary layer, associated with prevailing southwesterly winds (20–25 kt) at 800–500 hPa. Note that the layer between 925 and 850 hPa was saturated, which suggests limited solar heating and surface temperature increases for the day. At 1100 LST, the wind below 950 hPa turned northerly (Figure 3b), indicating the sea breeze penetrating the Taipei Basin. The moisture brought by the sea breeze and the surface warming due to diurnal heating led to a significant increase in CAPE to 2,600 J kg^{-1}, consistent with the results in Miao and Yang (2020).

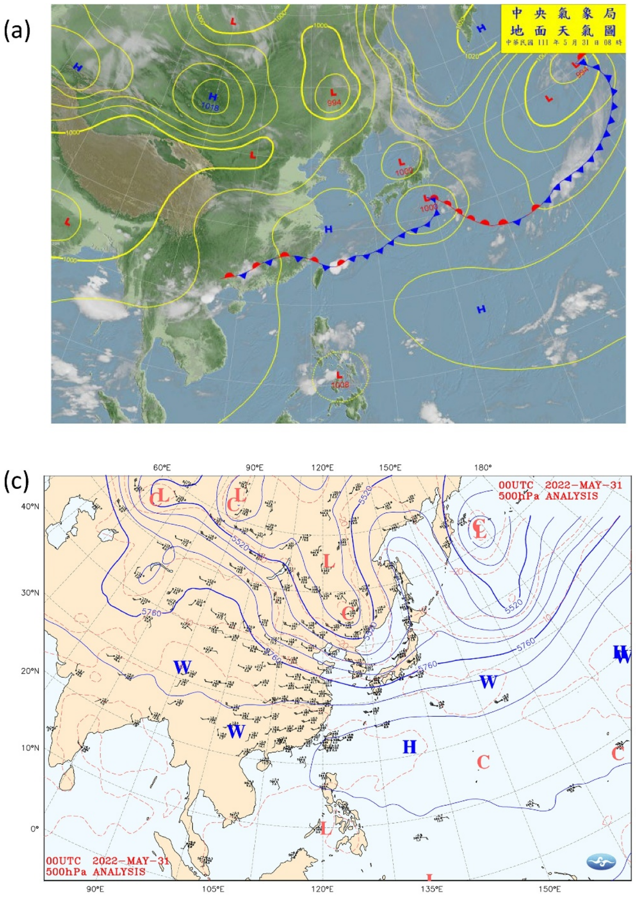

Figure 2. Synoptic condition at 0000 UTC (0800 LST) 31 May 2022: (a) CWB surface analysis map; (b) 850-hPa map with the geopotential height (solid contours), temperature (dashed contours), and horizontal wind barbs; (c) 500-hPa map; (d) 200-hPa map.

3.2. Storm Evolution

Convective cells initiated near the foothills of the Snow Mountain Range (SMR) around 1140 LST. Subsequently, the convection gradually evolved into an organized ATS system. Strong radar reflectivity values (>40 dBZ) mainly occurred over the SMR in the afternoon on 31 May 2022 (Figure 4a). In contrast, there was no significant signal of strong convection over the basin plain, which is different from a previously studied ATS case on 14 June 2015 (e.g., Miao & Yang, 2020; JJ23). There were two episodes of convection with ZH > 40 dBZ in this case (Figures 4b and 4c). Episode 1 occurred from 1200 to 1400 LST and Episode 2 occurred from 1500 to 1700 LST. The convection in both episodes propagated northeastward; however, the convection in Episode 1 exhibited a broader and more persistent region of strong reflectivity, indicating a higher degree of organization (1240–1330 LST; Figures 4b and 4c). Note that the convection was confined within the mountainous region (Figure 4c), resulting in heavy rainfall over the SMR but only weak rainfall over the basin plain.

To investigate the role of local circulation in this terrain-confined thunderstorm event, the evolution of reflectivity and multi-Doppler winds at 1.5 km AMSL is shown in Figure 5. It is clear that there were multiple mergers of convective cells in Episode 1. Following Miao and Yang (2018), a cell merger is defined as a situation when the 40-dBZ ZH radar contour connects at 1.5 km AMSL, lasting for at least 24 min. At 1200 LST, three convective cells, A, B, and C, were located at the foothills (Figure 5a). Subsequently, cells A and B merged and then intensified slightly (Figures 5b and 5c).

Southwesterly flow occurred over western SMR (<121.5°E) at 1200 LST, similar to the prevailing low-level winds shown by the sounding. On the other hand, southeasterly flow prevailed over the eastern SMR (>121.5°E), which appeared to be the upslope wind. Although cells A and B were located in an environment with southwesterly winds, the winds were weaker near cell B and even shifted to northwesterly at the foothills. The

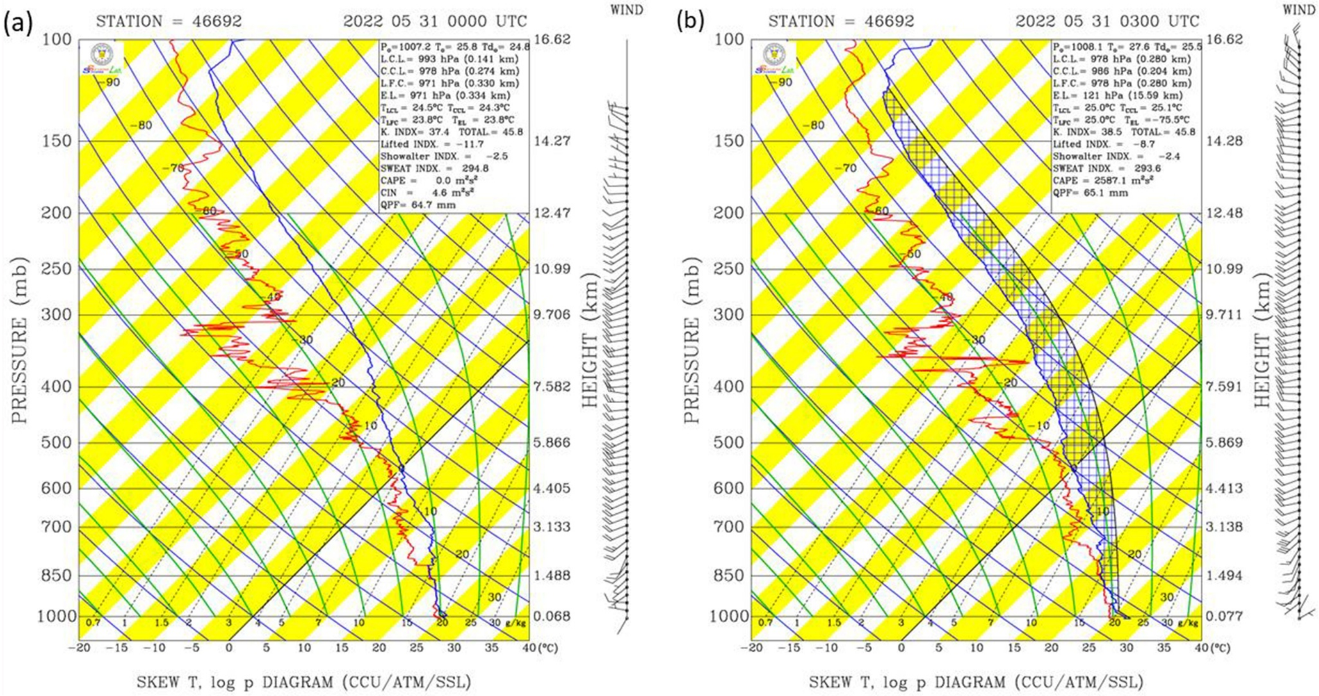

Figure 3. Soundings of temperature (blue line) and dew point (red line) at Banchiao station (46692) at (a) 0800 and (b) 1100 LST 31 May 2022. The location of Banchiao sounding station is shown in Figure 1.

difference in environmental wind speeds near cells A and B suggests that the physical mechanism of single cell merger (SCM; i.e., the merge of cells A and B) may be a "rear-end collision" type due to the different propagation speeds (Miao & Yang, 2018). It should be noted that the upslope (northwesterly) winds became more significant at the northwestern foothills in the SMR and converged with the southeasterly flow at 1236 LST, producing enhanced low-level convergence over the mountainous region. Cell A + B merged with cell C and formed a large area of strong reflectivity around 1248 LST (Figure 5d). After the multiple cell merger (MCM; the merger of A + B and C), the new convective cell A + B + C intensified significantly (Figure 5e). The orientation of the strong echoes and the enhanced low-level convergence region were both parallel to the SMR, implying that the

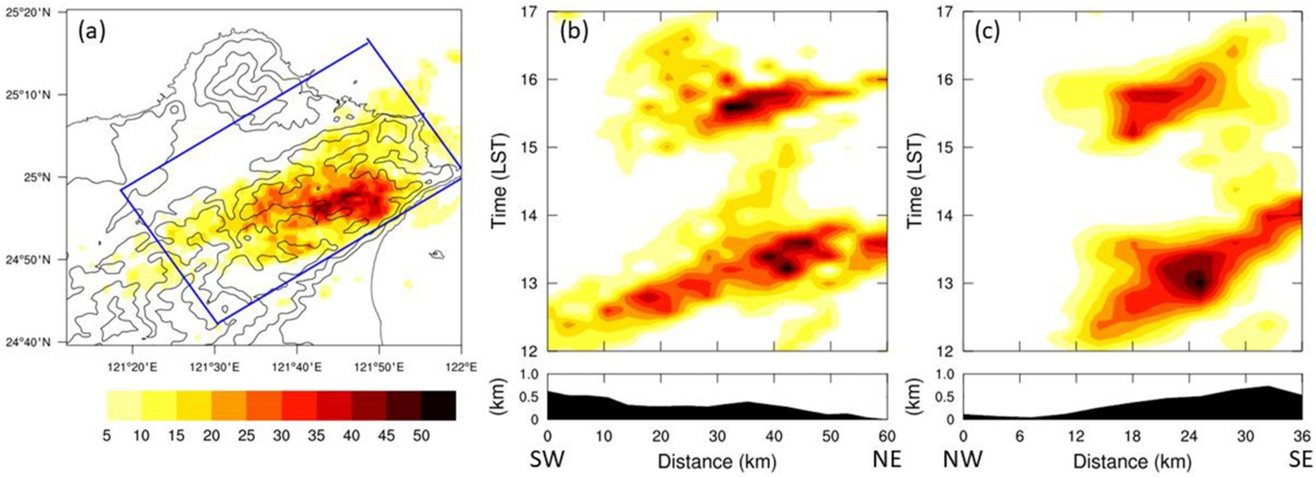

Figure 4. Temporal and spatial distribution of ZH at the height of 3 km above mean sea level on 31 May 2022. (a) Occurrence frequency (%) of ZH > 40 dBZ between 1200 and 1700 LST. Terrain heights are contoured by gray lines at 100, 300, 700, and 1,300 m. (b) The averaged spatial frequency of ZH > 40 dBZ along the southwest-northeast direction of the blue rectangle in (a). The average terrain height is indicated at the bottom. (c) As in (b), but along the northwest-southeast direction.

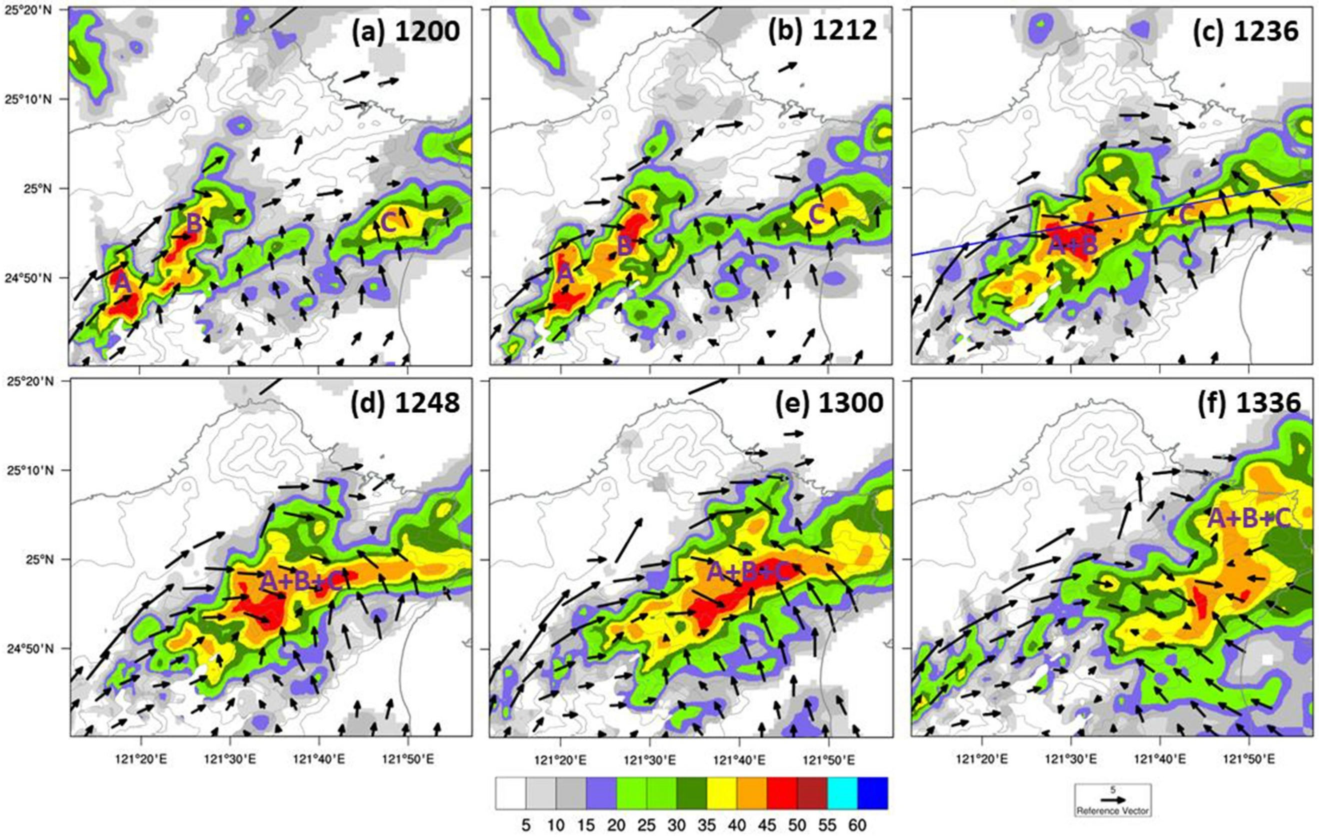

Figure 5. Constant-altitude plan position indicator of radar reflectivity at 1.5 km above mean sea level (AMSL) from S-Pol radar on 31 May 2022: (a) 1200 LST, (b) 1212 LST, (c) 1236 LST, (d) 1248 LST, (e) 1300 LST, and (f) 1336 LST. Multi-Doppler retrieved horizontal wind at 1.5 km AMSL (arrows) is also indicated. Terrain heights are contoured by gray lines at 100, 300, 700, and 1,300 m. Blue line in (c) shows the location of the vertical cross sections (S-Pol 78° RHI) in Figures 7–11. The convective cells A + B, C and A + B + C are labeled.

terrain might play an important role in this MCM event. Afterward, the merged cell propagated northeastward and weakened slightly at 1336 LST (Figure 5f).

The ATSs in Episode 2 showed a distinct multicellular structure (Figure 6). It is clear that convective cells in Episode 2 were more isolated and much weaker than in Episode 1. Moreover, there was no cell merger in Episode 2. Note that the enhanced low-level convergence over the SMR seen in Episode 1 was absent in Episode 2 (cf. Figures 5c and 6c). One reason for this difference could be a weaker temperature gradient from previous rainfall. Interestingly, there was a cyclonic circulation near the coastline in Yilan County at 1500 LST (Figure 6a), corroborated by NCEP FNL (Final) Operational Global Analysis (not shown). Afterward, this vortex appeared to form a closed circulation and moved northward during 1536–1600 LST (Figures 6b and 6c). Meanwhile, the easterly winds north of the vortex penetrated into the SMR. The convection over the SMR was located at the front of the advancing easterly winds and weakened gradually (Figures 6c and 6d). The comparison between Episodes 1 and 2 indicates that convective cells in Episode 2 were isolated and weaker in the absence of the enhanced upslope wind over the SMR region, suggesting the importance of thermally driven flow in convective organization and development.

4. Results

4.1. Episode 1: Multiple Cell Merger (MCM)

The detection of ZDR columns can be challenging due to operational radar resolution and storm motion effects (Snyder et al., 2015). To get an accurate quantification of ZDR columns, the evolution of RHIs from the S-Pol radar with an azimuth of 78° is shown in Figures 7–10. Luckily, these high-resolution RHI scans captured the merger of A + B and C in Episode 1, providing valuable insights into the MCM process.

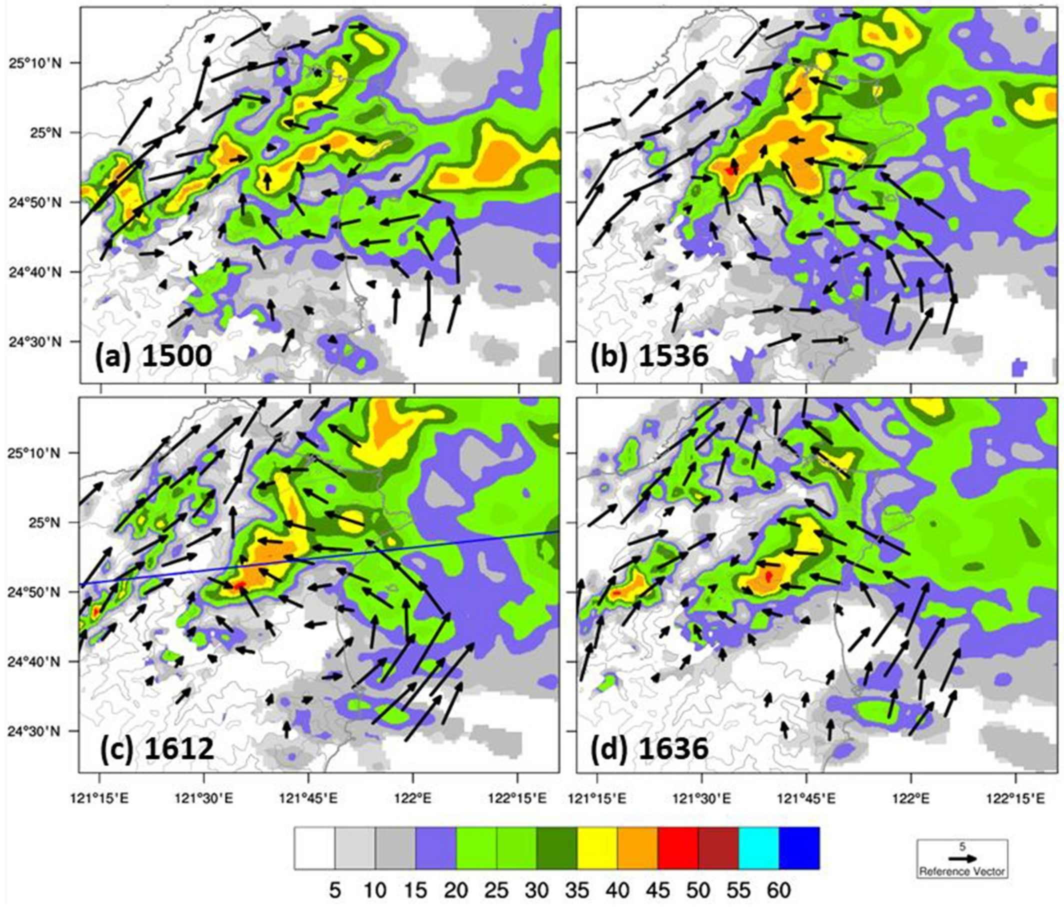

Figure 6. As Figure 5, but for (a)1500 LST, (b)1536 LST, (c)1612 LST, and (d)1636 LST. Note that the domain is larger than that in Figure 5 with terrain heights contoured by gray lines at 100, 700, 1,300, and 2,000 m. The blue line in (c) shows the location of the vertical cross sections (S-Pol 83° RHI) in Figures 12 and 13.

The reflectivity plot at 1223 LST (Figure 7a) shows the position and height of two convective cells A + B and C, with cell A + B exhibiting the stronger convection. Cell A + B had high ZH exceeding 55 dBZ and a 20-dBZ echo top of 14.5 km AMSL. The ZDR plot (Figure 8a) reveals ZDR columns in cells A + B and C at x (distance from the radar) = 60 km and x = 100 km, respectively, with heights reaching approximately 6 km, indicating the presence of convective updrafts. The ZDR value within the ZDR column of cell A + B ($x \sim 60$ km) is relatively large, with local maxima located at the middle (4–5 km AMSL) and low levels (<2 km AMSL). The area of high ZDR (>2.0 dB) values at middle levels corresponds to hail/rain and graupel/rain mixtures (Figure 10a). Additionally, the PID shows the presence of graupel and small hail in cell A + B at 5–10 km AMSL, suggesting ongoing riming processes and the presence of supercooled liquid water. The KDP plot (Figure 9a) reveals the existence of a KDP column coincident with a ZDR column (x = 60 km), which might be due to the low environmental wind shear (Kumjian & Ryzhkov, 2008). However, there is no prominent KDP column in cell C because it was relatively weak and had low liquid water content.

Note that at 1223 LST, developing cumulus and congestus clouds were observed between the two convective cells at x = 70–90 km. Subsequently (Figure 7b), these clouds extended above 8 km AMSL by 1235 LST. The cumulus and congestus clouds that developed between cells A + B and C coincided with the low-level convergence produced by upslope winds (Figure 5b), highlighting the role of terrain-induced circulation in this MCM process.

Before the merger, the 20-dBZ echo top only reached 14.5 km AMSL. After the merger of cells A + B and C, there was a significant increase in the horizontal and vertical extent of the high ZH (Figures 7c and 7d) with the echo top exceeding 16 km AMSL. After the MCM, the enhanced ZDR region (>1 dB) broadened, accompanied by the merger of ZDR columns (Figures 8c and 8d). The merged ZDR columns had a larger horizontal and vertical

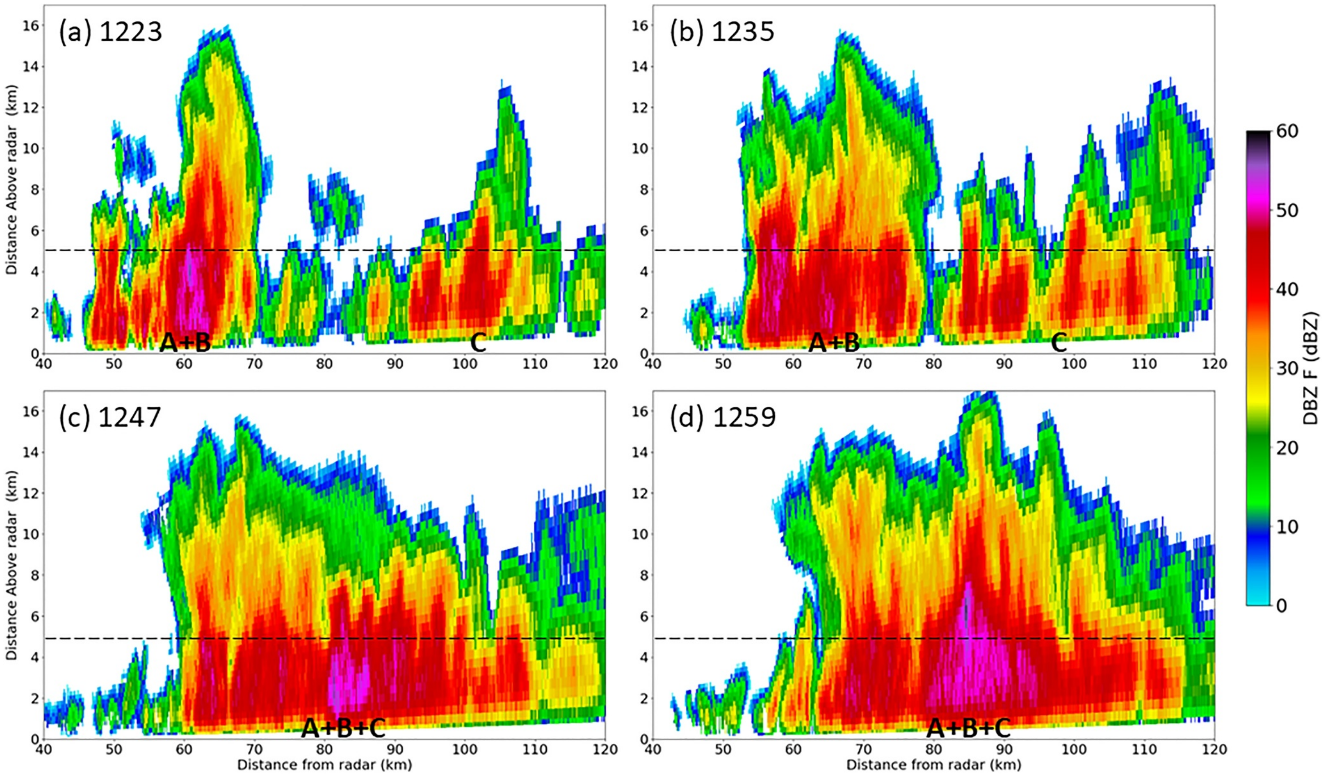

Figure 7. S-Pol range height indicator (azimuth angle 78°) of ZH on 31 May 2022: (a) 1223, (b) 1235, (c) 1247, and (d) 1259 LST. The convective cells A + B, C, and A + B + C are labeled. The dashed line represents the environmental 0°C level.

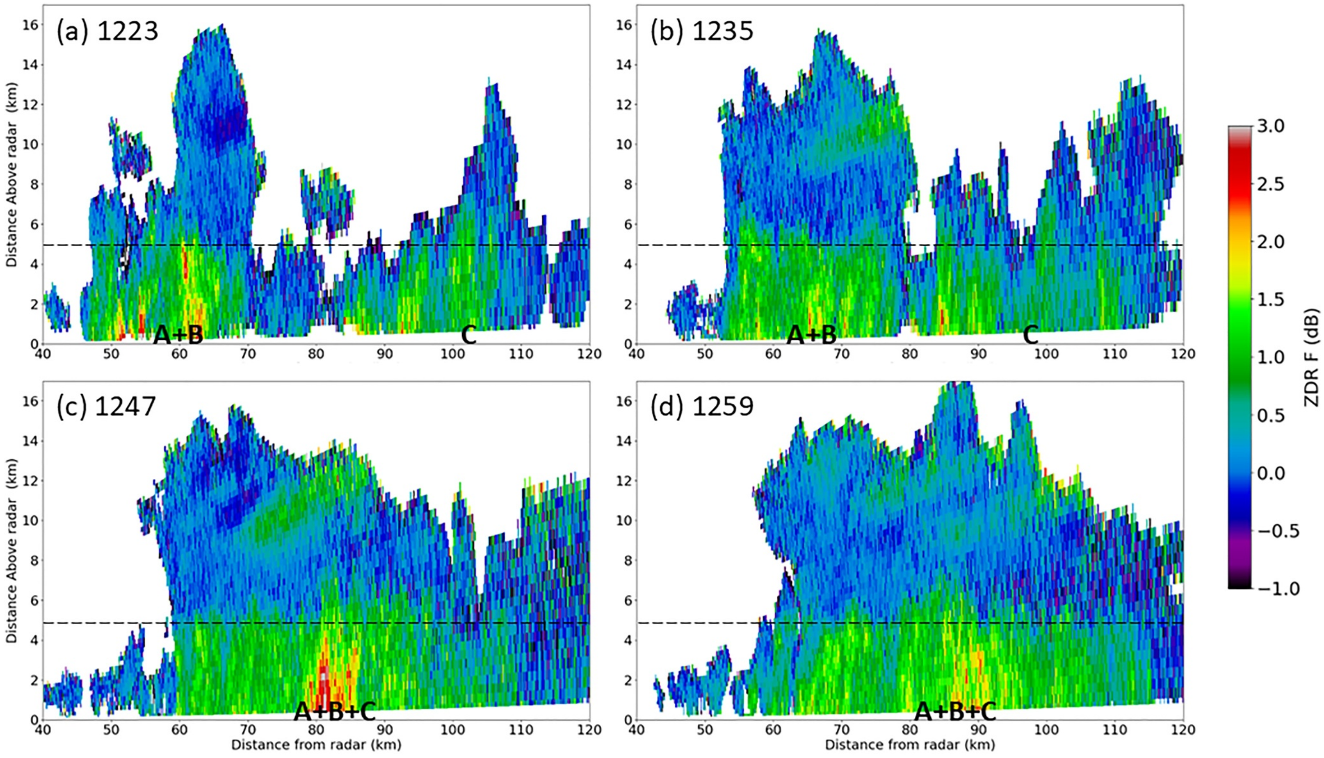

Figure 8. As Figure 7, but for ZDR.

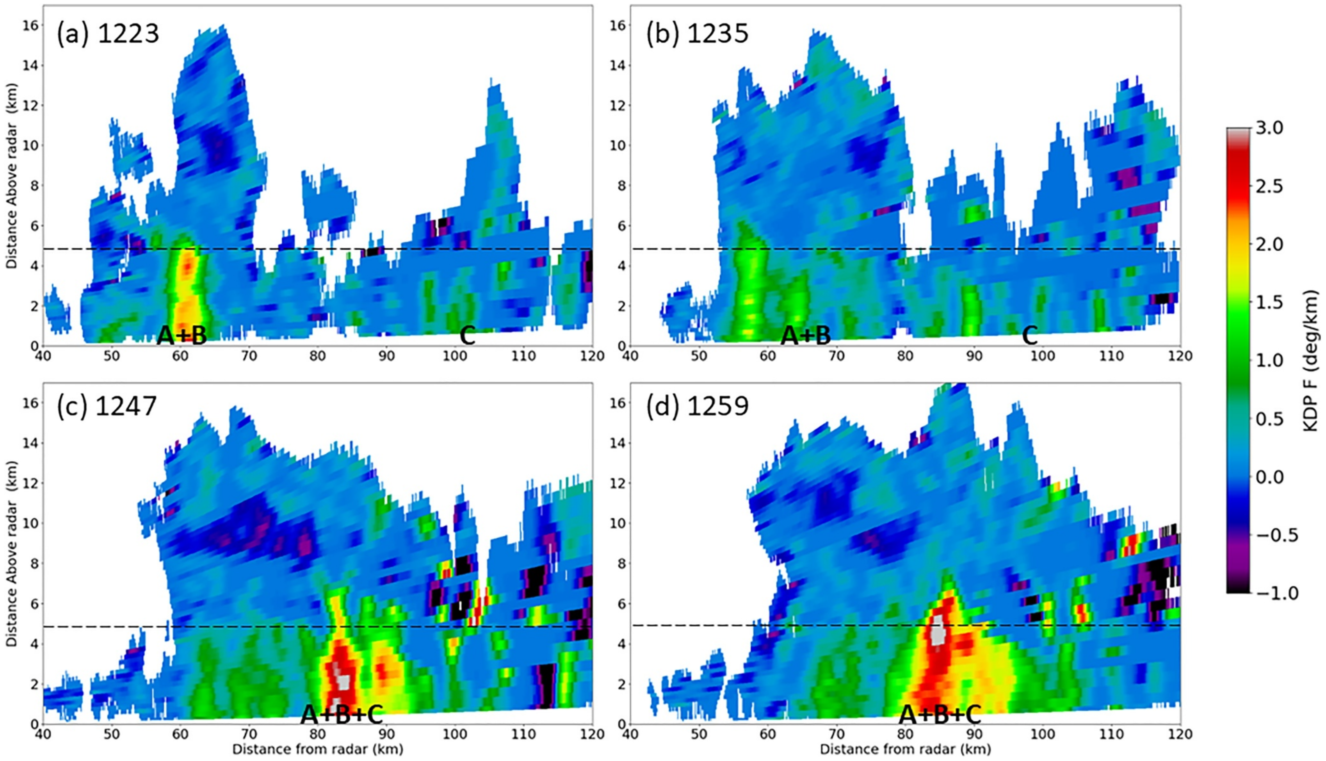

Figure 9. As Figure 7, but for KDP.

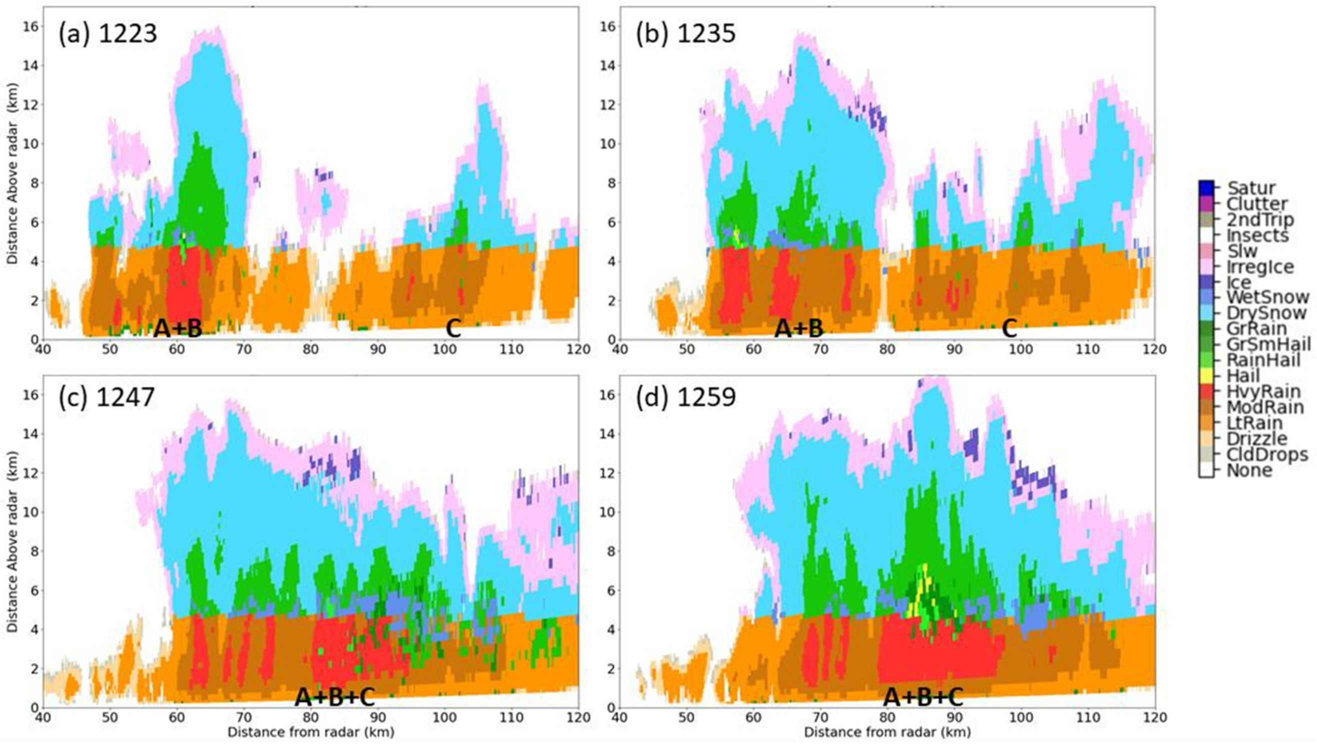

Figure 10. As Figure 7, but for particle identification.

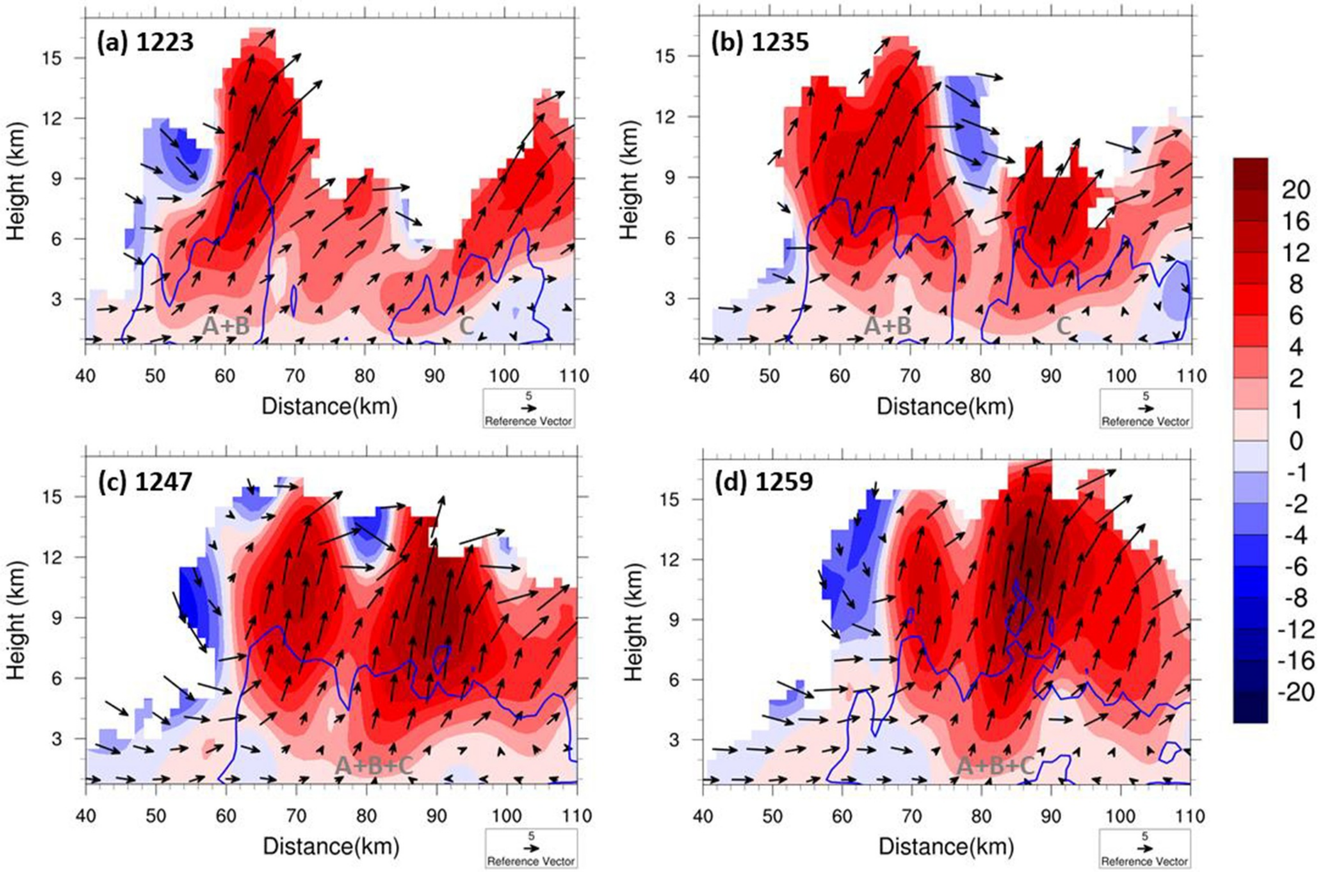

Figure 11. Evolution of retrieved winds (arrows) and vertical velocity (colored; in units of m s^{-1}) in cross-sections through the S-Pol 78° RHI: (a) 1223, (b) 1235, (c) 1247, and (d) 1259 LST. The radar reflectivity is contoured by blue lines at 35 dBZ. The convective cells A + B, C, and A + B + C are labeled.

extent than the isolated ZDR columns before the MCM process (Figures 8a and 8d). Since a ZDR column is a proxy for convective updrafts and its scale is correlated with updraft characteristics (Bringi et al., 1991; Kumjian et al., 2014), the occurrence of merged ZDR columns may suggest wider updrafts.

The KDP field at the time of the MCM (Figure 9c) showed a KDP column at $x = 84$ km with a height of 7 km AMSL (~2 km above the 0°C level). The maximum value of KDP (~3.5° km^{-1}) occurred below the melting level, and the magnitude was larger after the MCM process. The KDP column above the melting level was composed of abundant graupel, small hail, and rain/hail mixture (Figure 10c), indicating an active mixed-phase process. KDP was positively correlated with ZH in the merged cell below the melting level, likely because the bulk of graupel/hail melted into raindrops producing high KDP. Therefore, it can be inferred that active riming occurred above the melting level, and a large amount of graupel/hail melted into raindrops below the melting level.

At 1259 LST, the merged cell exhibited a maximum ZH of ~60 dBZ, signifying the presence of hail aloft (Figure 7d). ZDR and KDP columns were observed at $x = 85$ km with a height of about 7 km (~2 km above the 0°C level; Figures 8d and 9d). PID (Figure 10d) shows a significant increase in the horizontal extent of the graupel/small hail mixture and the height extended to 12 km AMSL. Furthermore, there was an increase in the occurrence of hail, rain/hail, and graupel/rain mixtures at $x \sim 80$–91 km. Some water-coated graupel and large supercooled raindrops may have produced high values of KDP (>2.5° km^{-1}) above the freezing level and formed the upper part of the KDP column (Ryzhkov & Zrnić, 2019). Below the melting level to a height of 3.5 km ($x = 80$–91 km), a large amount of graupel/rain and rain/hail mixture was observed, corresponding to high ZDR (>2 dB), possibly attributed to the large raindrops produced by the shedding and melting of graupel and hail.

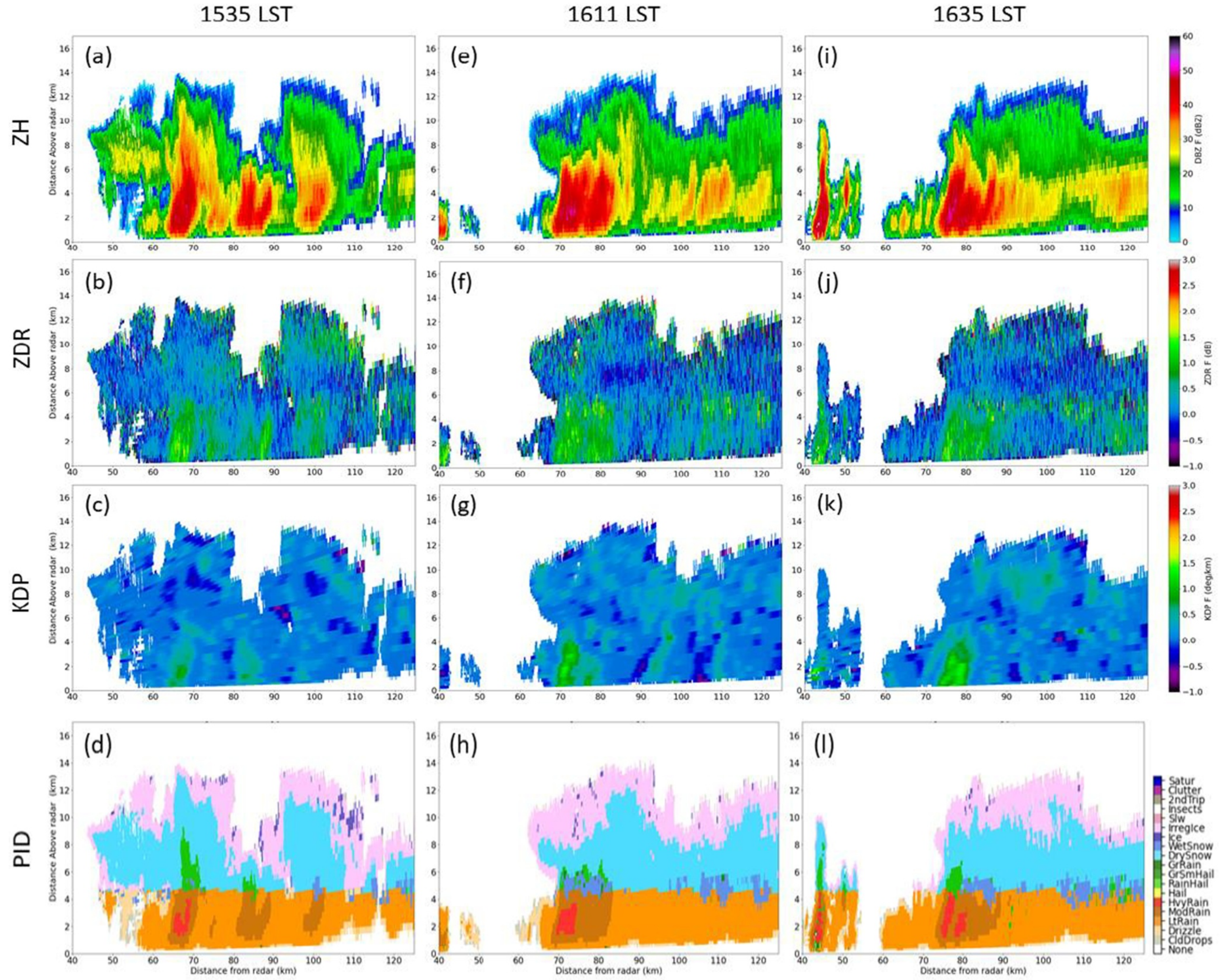

Figure 12. S-Pol range height indicator (azimuth angle 83°) of ZH, ZDR, KDP, and particle identification on 31 May 2022: (a)–(d) 1535 LST, (e)–(h) 1611 LST, and (i)–(l) 1635 LST.

Previous results show that microphysics in the merged cell transitioned to more active riming and melting processes. To shed more light on the storm kinematics and its connection with polarimetric signatures, multi-Doppler winds interpolated to the S-Pol 78° RHI position are shown in Figure 11 and provide valuable insights into cell merger dynamics. At 1223 LST, the retrieved updrafts match well with the ZDR columns of cells A + B and C at $x = 60$ and 100 km, respectively (Figures 8a and 11a). The upward motion between cells A + B and C was associated with the low-level convergence produced by upslope winds (Figure 5b). As the cells and associated updrafts became closer at 1235 LST, the compensating downdraft at the upper levels between them extended down to 8 km AMSL (Figure 11b).

Before the cell merger, the maximum vertical velocity w was ~12 m s^{-1}. The mid-to-upper-level updrafts (>4 m s^{-1}) merged and intensified dramatically to ~18 m s^{-1} while the cells A + B and C merged (Figure 11c). The wide and strong updraft following the MCM was associated with the merged ZDR columns, suggesting that merged ZDR columns may be a proxy for updraft mergers and convective organization, which has been less emphasized in previous studies. Subsequently, the strongest updraft reached up to 17 km AMSL with a maximum w of greater than 20 m s^{-1} (Figure 11d; $x \sim 85$ km), which was associated with the broad enhanced ZDR region (Figure 8d) and a large amount of hail and graupel (Figure 10d). The merged ZDR columns exhibited a broader horizontal extent compared to the isolated ZDR columns. This broader enhanced ZDR region may suggest a wider

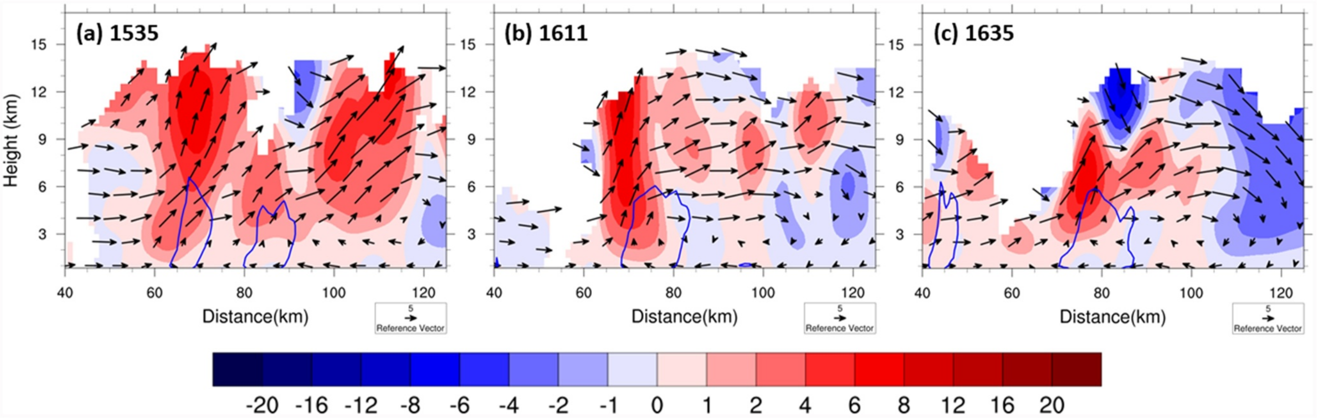

Figure 13. As Figure 11, but for the cross-sections through the S-Pol 83° RHI: (a) 1535, (b) 1611, and (c) 1635 LST.

updraft region, which could influence the microphysical pathways of ATS. Given the 12-min RHI update interval, this interpretation should be regarded as tentative.

4.2. Episode 2: Isolated Convective Cells

Figure 12 shows the evolution of ZH, ZDR, KDP, and PID in Episode 2. Convective cells in Episode 2 were more isolated and much weaker than those in Episode 1. The 20-dBZ echo top only reached 12 km AMSL in episode 2, whereas echo tops extended up to 16 km AMSL in Episode 1. At 1535 LST, the ATS system shows a multicellular structure (Figure 12a). Subsequently, the isolated cells propagated eastward and the front side of the system (Figures 12b and 12c; $x = 100$–125 km) gradually evolved into a stratiform region. The melting layer (~5 km AMSL) in the stratiform region was marked by a slight enhancement of ZDR and well-pronounced correlation coefficient (ρhv) minimum (not shown), although the ZH does not exhibit a clearly defined bright band.

In contrast to the ATS in Episode 1, there were no well-defined ZDR columns in most scans during Episode 2, likely due to relatively weak updrafts (cf. Figures 11 and 13). Accordingly, instead of graupel particles, there was a large amount of dry snow at mid-to-upper levels and wet snow near the melting level in Episode 2 (Figures 12d, 12h, and 12l). Compared to Episode 1, the area of heavy rainfall decreased noticeably in Episode 2, accompanied by much lower values of ZDR and KDP that might be due to the lack of large raindrops produced by melting hail and graupel.

In the absence of a cell and updraft merger, the updrafts showed a disorganized and slantwise structure with the maximum w of 8 m s^{-1} at 1535 LST (Figure 13a). Meanwhile, the aforementioned easterly flow was located below 2 km AMSL ($x \sim 90$–125 km). An hour later, this easterly flow advanced westward to $x \sim 75$ km (Figure 13c). It can be seen that the slantwise upward flow over the easterly flow weakened gradually and became downdrafts in the stratiform region.

4.3. Evolution of ZDR Column and Updraft

Thunderstorm updrafts are key areas for precipitation growth and electrification, making their accurate detection via radar data essential for assessing storm damage potential. Tracking the height of ZDR columns has been proposed for nowcasting thunderstorm evolution with lead times of 10–20 min (Kuster et al., 2019; Snyder et al., 2015). This study analyzes the temporal evolution of polarimetric signatures and updraft intensities to explore their relationship over complex terrain while acknowledging that the 12-min RHI update interval limits the ability to fully capture short-lived features.

Figures 14a and 14b show the time series of maximum height and width for the ZDR columns along S-Pol 78° RHI in Episode 1. Note that the width of the enhanced ZDR region (>1 dB) is computed at 5.5 km AMSL. Before the merger of cells A + B and C, the maximum height of ZDR columns was 6.0–6.5 km AMSL (~1.0–1.5 km above the 0°C level). It can be seen that the maximum height increased to 7.0 km AMSL around the merging time (1247 LST), indicating that the MCM process was accompanied by strong updrafts that lifted more supercooled

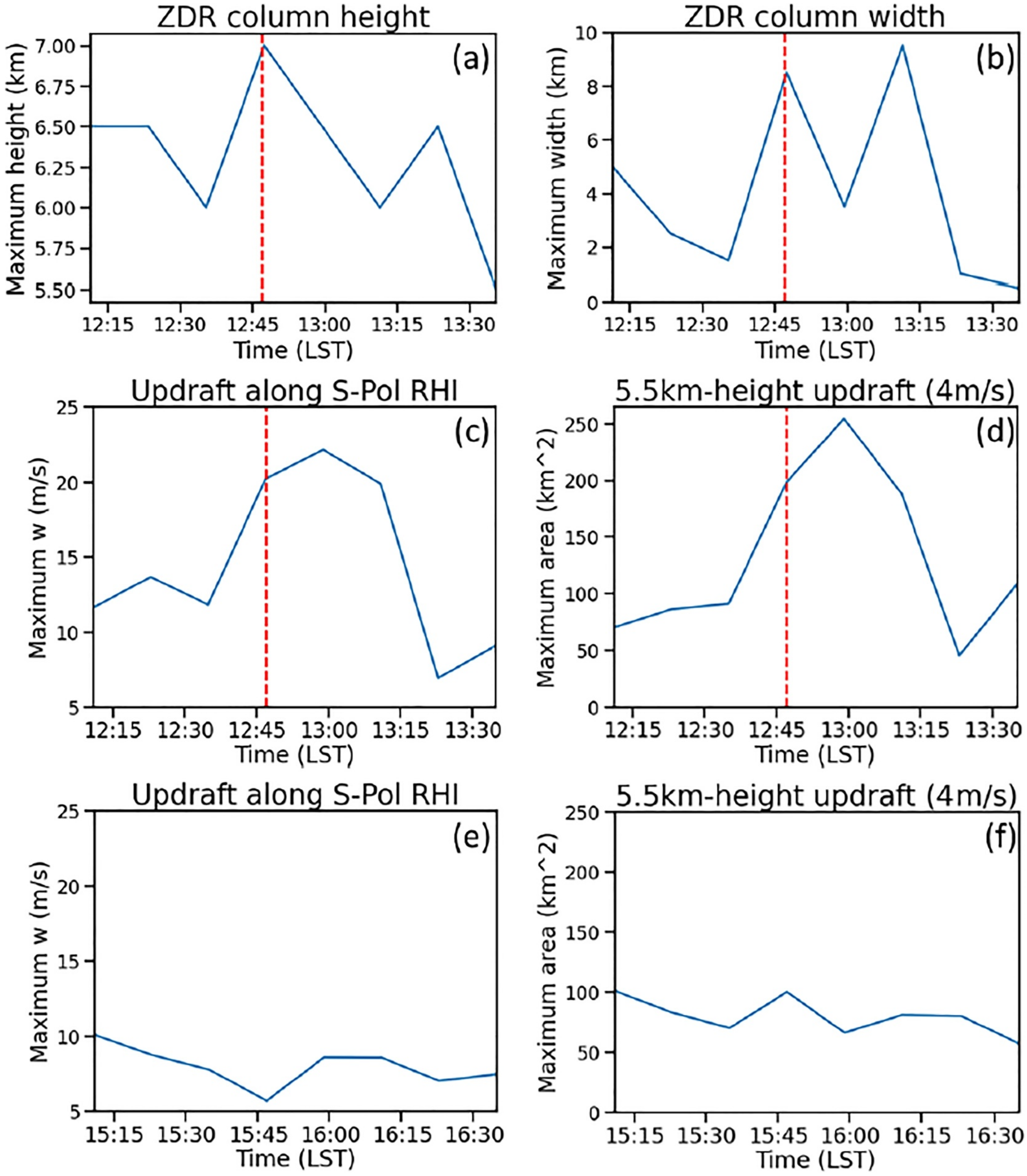

Figure 14. (a)–(d) Evolution during Episode 1: (a) maximum height and (b) maximum width of the ZDR columns along the S-Pol 78° RHI. (c) Maximum retrieved vertical velocity w of the updrafts along the S-Pol 78° RHI. (d) The maximum connected area of updrafts ($w > 4$ m/s) which is calculated at the 5.5 km above mean sea level (AMSL). The maximum width of ZDR columns is calculated at the 5.5 km AMSL. The time of merger of A + B and C is labeled as the red dashed lines. (e), (f) As (c), (d) except for Episode 2. Note that (e) is computed at S-Pol 83° RHI.

water above the melting level (Figure 11c). The maximum width of ZDR columns was ~5 km before cell merger. The width increased significantly to 8 km at the merging time, with an even broader width (~9.5 km) observed at 1311 LST, suggesting a wider updraft region. A temporary decrease in width occurred at 1259 LST, which might be attributed to the presence of hail (Kumjian et al., 2014). Afterward, the maximum width (height) of ZDR columns plummeted to ~0.5 km (5.5 km) at 1335 LST.

To investigate the relationship between ZDR columns and updraft intensity, Figures 14c and 14d show the maximum w along the S-Pol 78° RHI and the maximum connected area of updrafts with $w > 4 \text{ m s}^{-1}$ at 5.5 km AMSL in Episode 1. Both updraft velocities and areas rose rapidly at the merging time. The maximum updraft speed (area) increased from 13 m s^{-1} (90 km^2) to 22 m s^{-1} (250 km^2) after the MCM. Moreover, the updraft

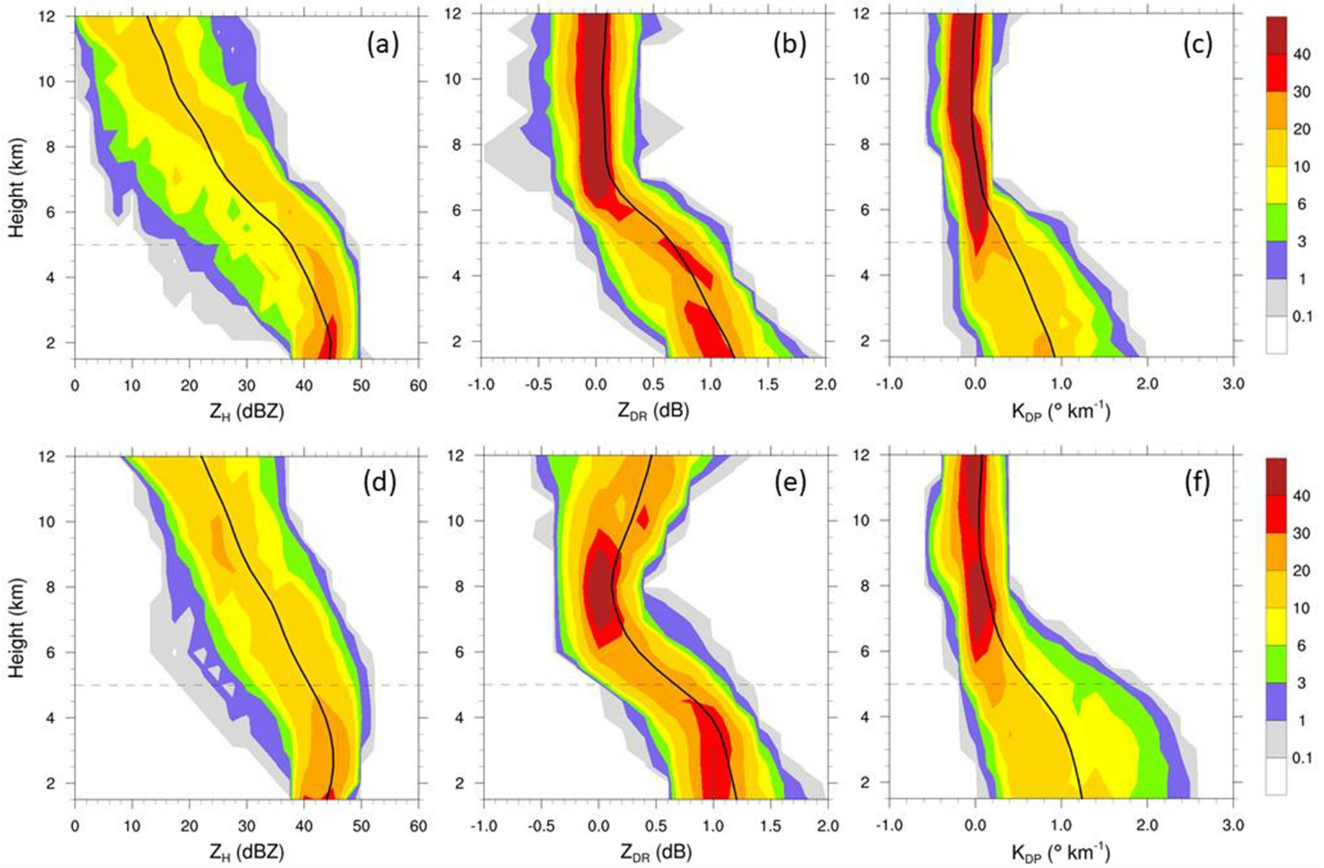

Figure 15. (a)–(c) CFADs (colored; in units of %) of (a) ZH, (b) ZDR, and (c) KDP within the 1.5-km-height strong echo region (>40 dBZ) over the Taipei Basin domain at 1224 LST. The CFAD percentages represent the relative frequency of each variable within a height bin, normalized by the total number of data points in that height bin. The mean profile is indicated as a black line in each panel. The environmental 0°C level is labeled as a dashed line. (d)–(f) As (a)–(c) except for 1300 LST. The CFADs are computed from the PPI scans of S-Pol.

velocity and area followed a similar evolution, seemingly related to the width of the ZDR column. After the merger, the horizontal extent of updrafts enlarged. Thus, the updraft core might have been less likely to be impacted by environmental dry air entrainment, which maintained the positive buoyancy and lead to the intensification of the merged cell (Miao & Yang, 2022).

In contrast to Episode 1, the convective cells were isolated, and no well-defined ZDR columns were observed in most scans during Episode 2 (Figures 12b, 12f, and 12j). The maximum updraft speed (<10 m s^{-1}) in Episode 2 was much lower than that in Episode 1 (Figures 14c and 14e). Moreover, the maximum updraft area (<100 km^2) was far smaller (Figures 14d and 14f). These results suggest that convective organization in the MCM process plays a critical role in the development of ATSs over the SMR, although short-lived features might have gone undetected due to the 12-min radar update time.

4.4. Evolution of Microphysical Processes

To further compare the bulk polarimetric features of the merged and isolated convective cells during Episodes 1 and 2, contoured frequency by altitude diagrams (CFADs; Yuter & Houze, 1995) of ZH, ZDR, and KDP in the tracked convective areas are presented in Figures 15 and 16. The maximum connected area of strong echo (>40 dBZ) at 1.5 km AMSL was tracked and the CFADs were computed within this area. First, we compare the vertical structure of polarimetric measurements in SCM (1224 LST) and MCM (1300 LST). The less intense and shallower convection in SCM had 1% of 35-dBZ reflectivity extending through 7.5 km AMSL (Figure 15a). The MCM with more intense and deeper convection had 1% of 35-dBZ reflectivity up to 12 km AMSL (Figure 15d).

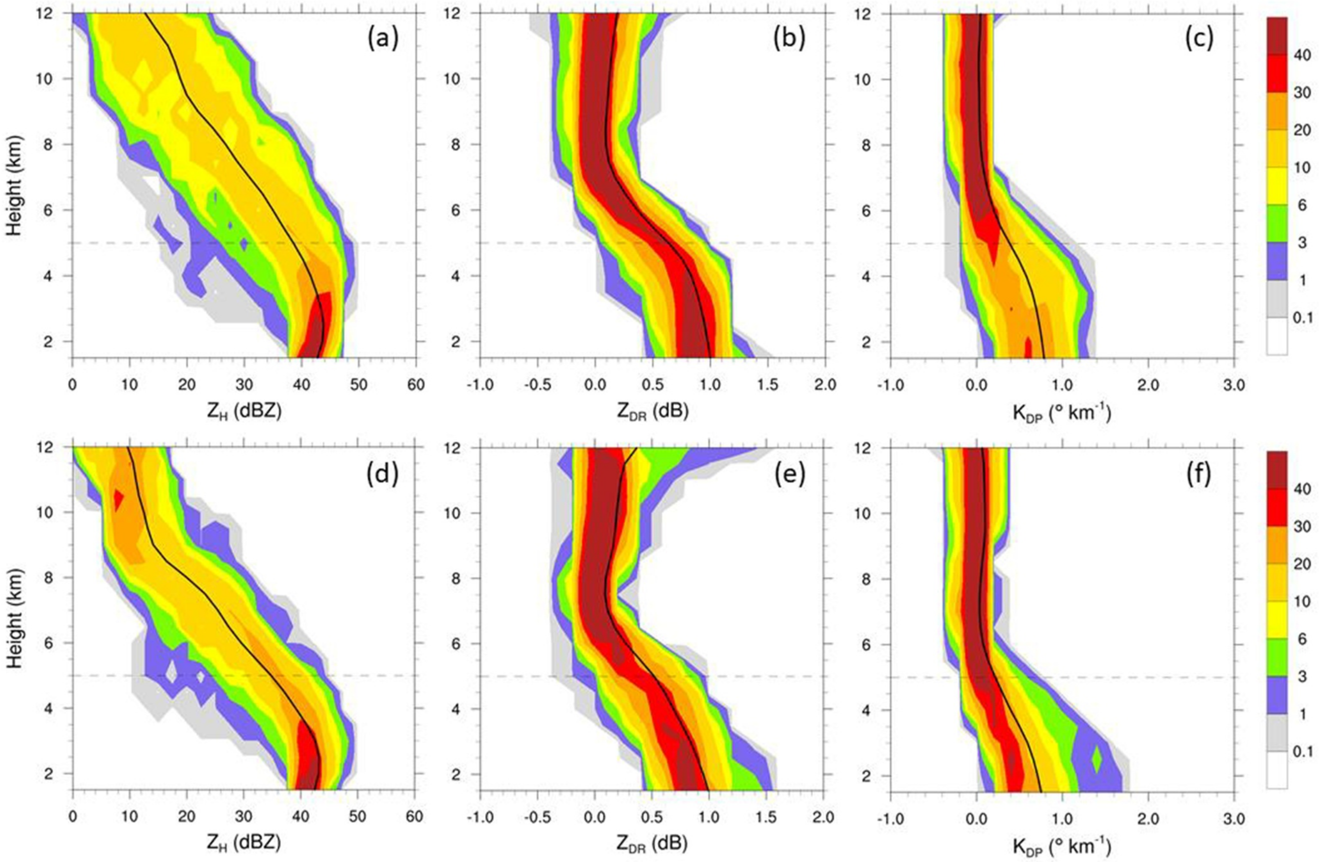

Figure 16. As Figure 15, but for (a)–(c) 1524 LST and (d)–(f) 1612 LST.

The mean ZH profile (Figures 15a and 15d) indicates higher values in MCM than SCM throughout the low to upper levels.

The 0.1% frequency contour of 1.0-dB ZDR extended to higher levels (6.5 km; Figure 15e) in MCM compared to SCM (6.0 km; Figure 15b). Moreover, 0.1% of 1-deg/km KDP also reached higher levels (7.0 km; Figure 15f) in MCM than SCM (6 km; Figure 15c). These results indicate more supercooled liquid droplets were lofted by

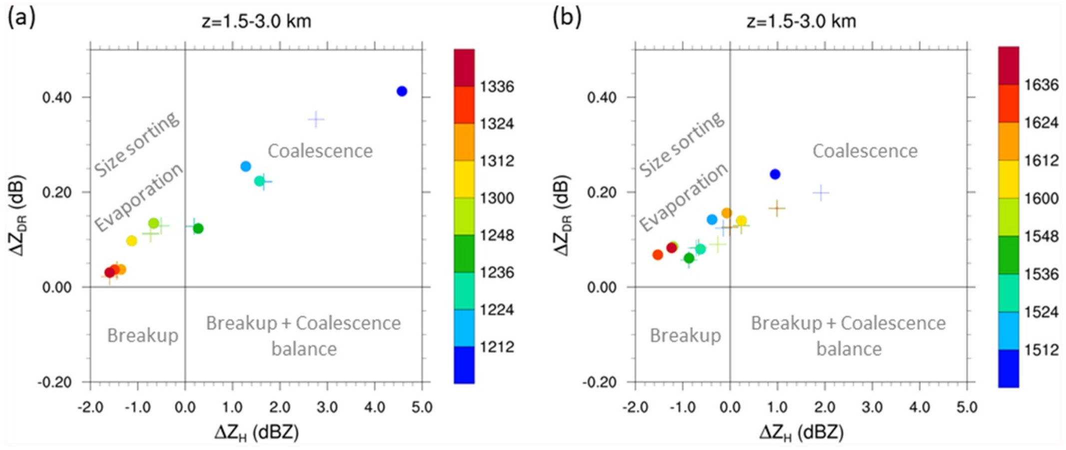

Figure 17. The change in ZDR as a function of the change in ZH from 3 to 1.5 km above mean sea level in the afternoon thunderstorms in the Eulerian (cross) and Lagrangian (circle) framework: (a) Episode 1 and (b) Episode 2. The microphysical processes represented by each quadrant are annotated. The colors of these symbols represent the observed time (LST).

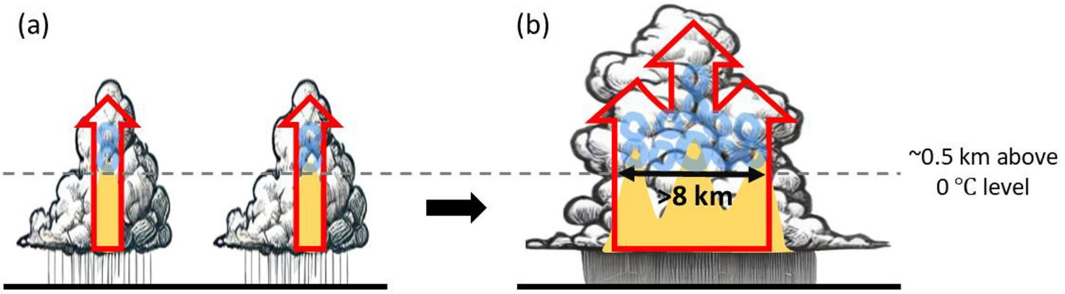

Figure 18. Conceptual diagram illustrating changes in ZDR column structure associated with multiple cell mergers. (a) Before the merger, individual convective cells contain distinct ZDR columns (yellow shading), each associated with localized updrafts (red arrows). (b) After multiple cell mergers, the updrafts merge, along with the development of a wide (>8 km) enhanced ZDR region (>1 dB) at 5.5 km altitude (~0.5 km above the environmental 0°C level). This structure indicates a larger, more organized updraft region with enhanced mixed-phased microphysical processes, including the lofting of graupel (blue circles) above the 0°C level.

stronger updrafts in MCM, which can enhance the riming and electrification processes (Takahashi, 1978; Kumjian & Ryzhkov, 2008; Mattos et al., 2017). Note that the 0.1% threshold highlights rare but significant radar features linked to the most intense updrafts during storm mergers, providing insights into kinematic differences between SCM and MCM. At 8–12 km AMSL, the majority of ZDR values were centered at ~0 dB and showed no noticeable vertical variation for SCM. On the other hand, the upper-level distribution of ZDR shifted to larger values (~0.5 dB) and displayed a significant downward decrease of ZDR between 8 and 12 km for MCM, which might be due to a more active riming process (Kumjian et al., 2022) or depolarization effect by oriented crystals (Ryzhkov & Zrnic, 2007). The downward increase of ZDR due to the melting of graupel was more pronounced near the 0°C level in MCM. Below the freezing level, the mean values of ZDR and KDP were higher in MCM, suggesting larger raindrops and higher rainwater content.

Secondly, we compare the profile of polarimetric variables between merged and isolated convection in Episodes 1 and 2, respectively. The 1% 35-dBZ reflectivity descended from 9 to 7 km (Figures 16a and 16d), suggesting the convection in Episode 2 weakened. In contrast to Episode 1, the heights of 0.1% 1-dB (deg km^{-1}) ZDR (KDP) were about 5 km or even lower (Figures 16b, 16c, 16e, and 16f), indicative of the much weaker updrafts in Episode 2 (Figure 14). At 8–12 km, the major distribution (>20%) of ZDR approached ~0 dB in Episode 2, suggesting no signal of active riming. At low levels, the mean value of ZDR (KDP) in Episode 2 was lower by ~17% (24%) than that in Episode 1, suggesting smaller raindrops and lower rainwater content.

Recent studies have utilized dual-polarization radar "fingerprints," specifically the vertical gradients of polarimetric variables, to infer dominant microphysical processes within storms (Kumjian et al., 2022). ZH and ZDR variations within the 1.5-km pure rain layer (1.5–3.0 km AMSL) provide insights into changes in raindrop size and number concentration, offering a way to infer dominant warm-rain processes such as coalescence, evaporation, size sorting, and breakup (Chen et al., 2019). Figure 17 illustrates the evolution of ZH and ZDR in this layer (1.5–3.0 km AMSL) over the strong echo (>40 dBZ) during Episodes 1 and 2. Each dot represents a radar volume scan, with color indicating the chronological order. Interestingly, the temporal evolution of the samples shows a distinct pathway from coalescence ($\Delta ZH > 0$ and $\Delta ZDR > 0$) to the evaporation/size sorting quadrant ($\Delta ZH < 0$ and $\Delta ZDR > 0$) during Episode 1 (Figure 17a). The samples in the SCM fall in the coalescence-dominant quadrant, indicating the importance of the coalescence process at low levels. Afterward, samples in the MCM are located in the top left quadrant, indicating the significant role of evaporation and size sorting in the later stage of the merged ATS system. In contrast, most of the samples are located in the evaporation/size sorting regime during Episode 2 (Figure 17b), indicating that evaporation processes are dominant at most of the time. Only few samples with low ΔZDR and low ΔZH fall in the coalescence quadrant, suggesting the limited coalescence process within isolated convection, which may be due to the weaker low-level convergence and updrafts in Episode 2.

In the tropical DYNAMO/ARM-AMIE data set of S-Pol observations, most of the convection cases reveal fingerprints for coalescence and evaporation, whereas many stratiform cases exhibit signatures of breakup, coalescence, and evaporation (Kumjian & Prat, 2014). They further suggest that the initial ZDR aloft is the primary indicator of the subsequent behavior of the rain shaft. Specifically, drop size distributions characterized by smaller drops initially (i.e., smaller initial ZDR) tend to lead to increases in ZDR over the rain shaft. Our study indicates that coalescence and evaporation are the dominant warm-rain processes in this terrain-confined ATS case in TAHOPE/PRECIP IOP 2, which is consistent with the results from Kumjian and Prat (2014) on the oceanic convection.

5. Discussion and Conclusions

This study investigates the microphysical and kinematic processes of severe ATSs of the IOP 2 in TAHOPE/PRECIP field campaigns utilizing the high-quality S-Pol radar observations and the multi-Doppler winds retrieved by SAMURAI-TERRAIN. RHI observations from the S-Pol radar provided detailed insights into the microphysical and kinematical characteristics of deep convection that were unavailable from previous studies in northern Taiwan. Complete 3D retrieved winds are obtained using both PPI and RHI radar data, providing valuable information about the dynamics of the ATSs. This aids in the analyses of the interaction between convective cells over complex terrain in northern Taiwan. It was found that there were two episodes of severe ATSs over the SMR south of the Taipei Basin. The main morphologic difference between the storms was the MCM in Episode 1 and the isolated convective cells in Episode 2.

In Episode 1, the physical mechanism of single cell merger (SCM; i.e., the merge of cells A and B) was likely rear-end collision due to different propagation speeds (Miao & Yang, 2018), whereas the multiple cell merger (MCM; i.e., the merge of cells A + B and C) was favored by terrain-induced circulation. The low-level convergence produced by upslope winds favored the development and organization of ATSs over the SMR. Wind retrievals indicate that updrafts merged near the time of the MCM, followed by intensification with maximum w exceeding 20 m s^{-1}. Furthermore, the multi-merger convection had a large region of graupel/small hail extending up to 12 km AMSL. In summary, cloud microphysics in the multiple-merger cell transitioned to more active riming and melting processes, leading to heavy rainfall over the mountainous region.

In contrast, convective cells in Episode 2 were isolated and much weaker than in Episode 1. In the absence of cell and updraft merger processes, the relatively weak updrafts showed a disorganized and slantwise structure with a maximum w of ∼10 m s^{-1}. Accordingly, instead of hail and graupel, there was a large amount of dry snow at mid-to-upper levels and wet snow near melting level in Episode 2. Compared to Episode 1, the area of heavy rainfall reduced noticeably in Episode 2, accompanied by much lower values of ZDR and KDP that might be due to the lack of large raindrops produced by melting of hail and graupel.

JJ23 investigated a severe ATS case on 14 June 2015 resulting in flash flooding in the Taipei metropolitan area, indicating that the development of convective cells from the foothill to the basin was favored by the enhanced low-level convergence produced by the downslope outflow boundary and sea breeze (Jou, 1994; Miao & Yang, 2020). In contrast to the 14 June 2015 case (see Figure 5b in JJ23), the convection in this case was confined to the mountainous region (Figure 4a), leading to extreme orographic rainfall over the SMR. Although the mechanism of cells A and B merger in this terrain-confined ATS system has been discussed in previous studies (Miao & Yang, 2018; Tao & Simpson, 1989), the subsequent A + B and C merger is closely related to the upslope wind. This finding provides a new insight into the cell merger mechanism that was not discussed in previous studies. The merging of cells A + B and C was preceded by a bridge of cumulus and congestus clouds, which was similar to the "cloud bridge" proposed by Tao and Simpson (1989) and might simply represent the importance of low-level convergence to the merging process. It is worth noting that the low-level convergence region was parallel to the orientation of the SMR (Figure 5c), implying the role of topography in convective organization. Furthermore, the cell separation distance before the MCM was ∼30–40 km (Figure 7a), which was longer than that in previous modeling (<10 km; Table 1 in Stalker & Knupp, 2003) and observational studies (e.g., ∼15–20 km in JJ23; ∼20 km in Wu et al., 2021). These results have highlighted the interesting possibility: Low-level convergence resulting from terrain-induced circulation may provide a forcing mechanism for the formation of convective cells with a longer cell separation distance for cell mergers over mountainous regions. It should be noted that some aspects of cell evolution in this study may have gone undetected due to the 12-min RHI update interval, and future work with high-temporal-resolution observations and numerical experiments is needed to validate these mechanisms and their sensitivity to terrain geometry.

Thunderstorm updrafts are crucial for precipitation growth and electrification, making their accurate detection vital for assessing storm damage potential. Tracking ZDR column heights and areas has been suggested for

Table 1
Summary of Key Time Series Characteristics Across Three Afternoon Thunderstorm Cases, Highlighting the Relationship Between Multiple Cell Merger, Updraft Intensity, and Precipitation Evolution

Case	Maximum vertical velocity (m/s)	Time lag from multiple cell merger to peak updraft (min)	Maximum 10-min accumulated rainfall (mm)	Time lag from multiple cell merger to peak rainfall (min)
0531	22	12	24.5	23–33
0623	27	36	35	47
0624	25	12	24.5	27

nowcasting thunderstorm evolution (French & Kingfield, 2021; Kuster et al., 2019; Snyder et al., 2015). This study investigates the relationship between ZDR column metrics and updraft intensities over the terrain near Taipei Basin. The high-resolution RHIs are utilized to measure the height and width of ZDR columns directly. While the 12-min update time limits the ability to resolve rapid changes, these observations still provide valuable information on the connection between ZDR column width and updraft intensity/size in Taiwan's orographic convection.

In Episode 1, the observed maximum height of the ZDR column (7.0 km) occurred at the timing of the MCM and appeared to precede the observed highest updraft speeds by more than 10 min. It is worth noting that the maximum width of ZDR columns increased significantly to 8 km at the merging time, consistent with the appearance of merged ZDR columns. After the MCM, a broader enhanced ZDR region (~9.5 km) was observed, associate with stronger updrafts (~22 m s^{-1}) and a larger updraft area (~250 km^2). In contrast, no well-defined ZDR columns were observed in most scans during Episode 2, and the observed maximum updraft speed (~10 m s^{-1}) and area (~100 km^2) in Episode 2 was much lower than in Episode 1.

The updraft velocity and area followed a similar evolution in Episode 1, seemingly related to the width of the enhanced ZDR region, highlighting that ZDR column width was a promising forecasting parameter for thunderstorm evolution and intensity. Furthermore, in northern Taiwan, merged ZDR columns may be a manifestation of the updraft merger process, suggesting less dilution of updraft buoyancy due to entrainment (Glenn & Krueger, 2017; Miao & Yang, 2022). Although previous research on thunderstorms over the Taipei Basin (e.g., JJ23) did not emphasize the broadening of the enhanced ZDR region during cell merger, this feature is discernible in their Figure 8 and is consistent with our observations. These findings suggest that forecasting heavy rainfall in ATSs could benefit from considering the ZDR column width, especially when combined with other polarimetric radar signatures. Monitoring both the height and width of the enhanced ZDR region offers valuable insights into updraft characteristics and storm intensity, expanding its potential applications.

To further examine the relationship between the MCM, updraft intensity, and precipitation evolution, we also analyze two additional ATS cases presented in the supporting information and develop a conceptual diagram of the MCM based on all three cases in northern Taiwan (Figure 18). Across all three cases, a broadening of the enhanced ZDR region beyond 8 km at 5.5 km AMSL was observed during the MCM (Figure 14b, Figures S4b and S8b in Supporting Information S1), despite the 12-min RHI update time. The key time series characteristics from these cases are summarized in Table 1. The results indicate that the observed maximum vertical velocity following the MCM exceeded 22 m s^{-1} in all cases, with the highest reaching 27 m s^{-1} on 23 June. The time lag between the MCM and observed peak updraft velocity ranged from 12 to 36 min. The maximum 10-min accumulated rainfall exceeded 24 mm in all cases, with the 23 June case reaching 35 mm. The peak precipitation occurred 23–47 min after the MCM. These findings suggest that the MCM, along with the broadening of the enhanced ZDR region (>8 km), tends to precede intense updrafts and heavy rainfall.

This work builds on recent studies that examined ZDR column size in different geographic settings, such as Kuster et al. (2019) and French and Kingfield (2021). Although those studies focused on the relationship between ZDR column area and severe weather in the US, our research suggests that wide, merged ZDR columns may be relevant to severe storms over complex terrain in Taiwan, highlighting their potential utility as indicators of convective organization. However, this study is subject to limitations, particularly the 12-min radar update interval, which introduces uncertainty when interpreting rapidly evolving convective features. Although our three case studies support the value of ZDR column width as a diagnostic metric, further validation is needed to assess its broader applicability. Future work will extend this analysis to the entire TAHOPE/PRECIP data set to evaluate whether the ZDR column size reliably indicates storm intensification across a wider range of convective environments.

Data Availability Statement

The S-Pol radar observations analyzed in this study can be accessed through the NCAR Earth Observing Laboratory repository (NCAR/EOL S-Pol Team, 2023) at https://doi.org/10.26023/QA4M-CDHH-MY0Z. The Py-ART (Helmus & Collis, 2016) and LROSE (DeHart et al., 2024) for radar data processing and analysis are available at https://arm-doe.github.io/pyart/ and https://doi.org/10.5281/zenodo.11479603, respectively. The tobac (Heikenfeld et al., 2019) for tracking and object-based analysis is available on GitHub at https://github.com/tobac-project/tobac and on Zenodo at https://doi.org/10.5281/zenodo.8164675 (tobac Community et al., 2023). The synoptic weather maps and sounding plots during TAHOPE campaign are available at https://exp.pccu.edu.tw/TAHOPE_2022/ and http://140.137.32.27/exp/tahope/.

Acknowledgments

The authors thank Prof. Ben Jong-Dao Jou, Dr. Wen-Chau Lee, Prof. Angela Rowe, Dr. Chi-June Jung, and Mr. Frederick Iat-Hin Tam for their valuable feedback on this study. The authors also thank all the participants of the TAHOPE/PRECIP/T-PARCII campaigns for their diligent efforts in collecting the observational data. The constructive comments from anonymous reviewers that greatly improved the quality of our manuscript are deeply appreciated. Jyong-En Miao was supported by the National Science and Technology Council (NSTC) Graduate Students Study Abroad Program from Taiwan (Grant# NSTC 113-2917-I-002-051) during an 11-month research visit to Colorado State University. Ming-Jen Yang was supported by the National Science and Technology Council in Taiwan under Grant# NSTC 113-2111-M-002 -011.

References

Bell, M. M., Montgomery, M. T., & Emanuel, K. A. (2012). Air–sea enthalpy and momentum exchange at major hurricane wind speeds observed during CBLAST. *Journal of the Atmospheric Sciences*, *69*(11), 3197–3222. https://doi.org/10.1175/jas-d-11-0276.1

Bodine, D. J., & Rasmussen, K. L. (2017). Evolution of mesoscale convective system organizational structure and convective line propagation. *Monthly Weather Review*, *145*(9), 3419–3440. https://doi.org/10.1175/mwr-d-16-0406.1

Bringi, V. N., Chandrasekar, V., Meischner, P., Hubbert, J., & Golestani, Y. (1991). Polarimetric radar signatures of precipitation at S- and C-bands. *IEE Proceedings F (Radar and Signal Processing)*, *138*, 109–119. https://doi.org/10.1049/ip-f-2.1991.0017

Bringi, V. N., Knupp, K., Detwiler, A., Liu, L., Caylor, I. J., & Black, R. A. (1997). Evolution of a Florida thunderstorm during the convection and precipitation/electrification experiment: The case of 9 August 1991. *Monthly Weather Review*, *125*, 2131–2160. https://doi.org/10.1175/1520-0493(1997)125<2131:eoaftd>2.0.co;2

Carey, L. D., & Rutledge, S. A. (2000). The relationship between precipitation and lightning in tropical island convection: A C-band polarimetric radar study. *Monthly Weather Review*, *128*(8), 2687–2710. https://doi.org/10.1175/1520-0493(2000)128<2687:trbpal>2.0.co;2

Cha, T., & Bell, M. M. (2023). Three-dimensional variational multi-doppler wind retrieval over complex terrain. *Journal of Atmospheric and Oceanic Technology*, *40*(11), 1381–1405. https://doi.org/10.1175/JTECH-D-23-0019.1

Chang, P., Zhang, J., Tang, Y. S., Tang, L., Lin, P. F., Langston, C., et al. (2021). An operational multi-radar multi-sensor QPE system in Taiwan. *Bulletin America Meteorology Social*, *102*(3), E555–E577. https://doi.org/10.1175/BAMS-D-20-0043.1

Chang, W., Lee, W., & Liou, Y. (2015). The kinematic and microphysical characteristics and associated precipitation efficiency of subtropical convection during SoWMEX/TiMREX. *Monthly Weather Review*, *143*(1), 317–340. https://doi.org/10.1175/MWR-D-14-00081.1

Chen, G., Zhao, K., Wen, L., Wang, M., Huang, H., Wang, M., et al. (2019). Microphysical characteristics of three convective events with intense rainfall observed by polarimetric radar and disdrometer in eastern China. *Remote Sensing*, *11*(17), 2004. https://doi.org/10.3390/rs11172004

Chen, T., Wang, S., & Yen, M. (2007). Enhancement of afternoon thunderstorm activity by urbanization in a valley: Taipei. *Journal of Applied Meteorology and Climatology*, *46*(9), 1324–1340. https://doi.org/10.1175/jam2526.1

Cornejo, I. C., Rowe, A. K., Rasmussen, K. L., & DeHart, J. C. (2024). Orographic controls on extreme precipitation associated with a Mei-Yu front. *Monthly Weather Review*, *152*(2), 531–551. https://doi.org/10.1175/MWR-D-23-0170.1

DeHart, J., Dixon, M., Javornik, B., Bell, M., Cha, T.-Y., DesRosiers, A., & Lee, W.-C. (2024). nsf-lrose/lrose-releases: Lrose-jade-20230814 (lrose-jade-20230814) [Software]. *Zenodo*. https://doi.org/10.5281/zenodo.11479603

Doswell, C. A., Brooks, H. E., & Maddox, R. A. (1996). Flash flood forecasting: An ingredients-based methodology. *Weather and Forecasting*, *11*(4), 560–581. https://doi.org/10.1175/1520-0434(1996)011<0560:FFFAIB>2.0.CO;2

Du, Y., Chen, G., Han, B., Bai, L., & Li, M. (2020). Convection initiation and growth at the coast of south China. Part II: Effects of the terrain, coastline, and cold pools. *Monthly Weather Review*, *148*(9), 3871–3892. https://doi.org/10.1175/MWR-D-20-0090.1

Foerster, A. M., & Bell, M. M. (2017). Thermodynamic retrieval in rapidly rotating vortices from multiple-doppler radar data. *Journal of Atmospheric and Oceanic Technology*, *34*(11), 2353–2374. https://doi.org/10.1175/jtech-d-17-0073.1

French, M. M., & Kingfield, D. M. (2021). Tornado formation and intensity prediction using polarimetric radar estimates of updraft area. *Weather and Forecasting*, *36*, 2211–2231. https://doi.org/10.1175/WAF-D-21-0087.1

Glenn, I. B., & Krueger, S. K. (2017). Connections matter: Updraft merging in organized tropical deep convection. *Geophysical Research Letters*, *44*(13), 7087–7094. https://doi.org/10.1002/2017gl074162

Heikenfeld, M., Marinescu, P. J., Christensen, M., Watson-Parris, D., Senf, F., van den Heever, S. C., & Stier, P. (2019). Tobac 1.2: Towards a flexible framework for tracking and analysis of clouds in diverse datasets. *Geoscientific Model Development*, *12*(11), 4551–4570. https://doi.org/10.5194/gmd-12-4551-2019

Helmus, J. J., & Collis, S. M. (2016). The python ARM radar toolkit (Py-ART), a library for working with weather radar data in the python programming language. *Journal of Open Research Software*, *4*(1), e25. https://doi.org/10.5334/jors.119

Houze, R. A., Jr. (2012). Orographic effects on precipitating clouds. *Review of Geophysics*, *50*(1), RG1001. https://doi.org/10.1029/2011RG000365

Huang, Y., Liu, Y., Liu, Y., Li, H., & Knievel, J. C. (2019). Mechanisms for a record-breaking rainfall in the coastal metropolitan city of Guangzhou, China: Observation analysis and nested very large eddy simulation with the WRF model. *Journal of Geophysical Research: Atmospheres*, *124*(3), 1370–1391. https://doi.org/10.1029/2018JD029668

Illingworth, A. J., Goddard, W., & Cherry, S. (1987). Polarization radar studies of precipitation development in convective storms. *Quarterly Journal of the Royal Meteorological Society*, *113*(476), 469–489. https://doi.org/10.1002/qj.49711347604

Jou, B. J.-D. (1994). Mountain-originated mesoscale precipitation system in northern Taiwan: A case study of 21 June 1991. *Terrestrial, Atmospheric and Oceanic Sciences*, *5*(2), 169–197. https://doi.org/10.3319/tao.1994.5.2.169(tamex)

Jou, B.-J. D., Kao, Y.-C., Hsiu, R. R.-G., Jung, U. C.-J., Lee, J.-R., & Kuo, H.-C. (2016). Observational characteristics and forecast challenge of Taipei flash flood afternoon thunderstorm: Case study 14 June 2015. *Atmospheric Science*, *44*, 57–82. (in Chinese with English abstract).

Jung, C., & Jou, B. J. (2023). Bulk microphysical characteristics of a heavy-rain complex thunderstorm system in the Taipei basin. *Monthly Weather Review*, *151*(4), 877–896. https://doi.org/10.1175/MWR-D-22-0078.1

Klaus, V., Rieder, H., & Kaltenböck, R. (2023). Insights in hailstorm dynamics through polarimetric high-resolution X-band and operational C-band radar: A case study for Vienna, Austria. *Monthly Weather Review*, *151*, 913–929. https://doi.org/10.1175/MWR-D-22-0185.1

Kumjian, M. R., Khain, A. P., Benmoshe, N., Ilotoviz, E., Ryzhkov, A. V., & Phillips, V. T. J. (2014). The anatomy and physics of ZDR columns: Investigating a polarimetric radar signature with a spectral bin microphysical model. *Journal of Applied Meteorology and Climatology*, *53*(7), 1820–1843. https://doi.org/10.1175/JAMC-D-13-0354.1

Kumjian, M. R., & Prat, O. P. (2014). The impact of raindrop collisional processes on the polarimetric radar variables. *Journal of the Atmospheric Sciences*, *71*(8), 3052–3067. https://doi.org/10.1175/JAS-D-13-0357.1

Kumjian, M. R., Prat, O. P., Reimel, K. J., van Lier-Walqui, M., & Morrison, H. C. (2022). Dual-polarization radar fingerprints of precipitation physics: A review. *Remote Sensing*, *14*(15), 3706. https://doi.org/10.3390/rs14153706

Kumjian, M. R., & Ryzhkov, A. V. (2008). Polarimetric signatures in supercell thunderstorms. *Journal of Applied Meteorology and Climatology*, *47*(7), 1940–1961. https://doi.org/10.1175/2007JAMC1874.1

Kumjian, M. R., & Ryzhkov, A. V. (2012). The impact of size sorting on the polarimetric radar variables. *Journal of the Atmospheric Sciences*, *69*(6), 2042–2060. https://doi.org/10.1175/jas-d-11-0125.1

Kuster, C. M., Snyder, J. C., Schuur, T. J., Lindley, T. T., Heinselman, P. L., Furtado, J. C., et al. (2019). Rapid-update radar observations of ZDR column depth and its use in the warning decision process. *Weather and Forecasting*, *34*(4), 1173–1188. https://doi.org/10.1175/WAF-D-19-0024.1

Lee, M.-T., Lin, P.-L., Chang, W.-Y., Seela, B. K., & Janapati, J. (2019). Microphysical characteristics and types of precipitation for different seasons over North Taiwan. *Journal of the Meteorological Society of Japan*, *97*(4), 841–865. https://doi.org/10.2151/jmsj.2019-048

Li, H., Huang, Y., Hu, S., Wu, N., Liu, X., & Xiao, H. (2021). Roles of terrain, surface roughness, and cold pool outflows in an extreme rainfall event over the coastal region of South China. *Journal of Geophysical Research: Atmospheres*, *126*(23), e2021JD035556. https://doi.org/10.1029/2021JD035556

Loney, M. L., Zrnić, D. S., Straka, J. M., & Ryzhkov, A. V. (2002). Enhanced polarimetric radar signatures above the melting level in a supercell storm. *Journal of Applied Meteorology*, *41*(12), 1179–1194. https://doi.org/10.1175/1520-0450(2002)041<1179:eprsat>2.0.co;2

Mattos, E. V., Machado, L. A. T., Williams, E. R., Goodman, S. J., Blakeslee, R. J., & Bailey, J. C. (2017). Electrification life cycle of incipient thunderstorms. *Journal of Geophysical Research: Atmospheres*, *122*, 4670–4697. https://doi.org/10.1002/2016JD025772

Miao, J., & Yang, M. (2022). The impacts of midlevel moisture on the structure, evolution, and precipitation of afternoon thunderstorms: A real-case modeling study at Taipei on 14 June 2015. *Journal of the Atmospheric Sciences*, *79*(7), 1837–1857. https://doi.org/10.1175/JAS-D-21-0257.1

Miao, J.-E., & Yang, M.-J. (2018). Cell merger and heavy rainfall of the severe afternoon thunderstorm event at Taipei on 14 June 2015. *Atmospheric Science*, *46*, 427–453. (in Chinese with English abstract). https://doi.org/10.3966/025400022018124604004

Miao, J.-E., & Yang, M.-J. (2020). A modeling study of the severe afternoon thunderstorm event at Taipei on 14 June 2015: The roles of sea breeze, microphysics, and terrain. *Journal of the Meteorological Society of Japan*, *98*(1), 129–152. https://doi.org/10.2151/jmsj.2020-008

Morrison, H., van Lier-Walqui, M., Fridlind, A. M., Grabowski, W. W., Harrington, J. Y., Hoose, C., et al. (2020). Confronting the challenge of modeling cloud and precipitation microphysics. *Journal of Advances in Modeling Earth Systems*, *12*(8), e2019MS001689. https://doi.org/10.1029/2019MS001689

Moseley, C., Hohenegger, C., Berg, P., & Haerter, J. O. (2016). Intensification of convective extremes driven by cloud–cloud interaction. *Nature Geoscience*, *9*(10), 748–752. https://doi.org/10.1038/ngeo2789

NCAR/EOL S-Pol Team. (2023). Precip: NCAR S-Pol radar moments data. Version 1.0 [Dataset]. *UCAR/NCAR–Earth Observing Laboratory*. https://doi.org/10.26023/QA4M-CDHH-MY0Z

Picca, J., & Ryzhkov, A. (2012). A dual-wavelength polarimetric analysis of the 16 May 2010 Oklahoma city extreme hailstorm. *Monthly Weather Review*, *140*(4), 1385–1403. https://doi.org/10.1175/MWR-D-11-00112.1

PRECIP. (2022). Prediction of rainfall extremes campaign in the Pacific. Retrieved from http://precip.org/

Ryzhkov, A. V., & Zrnic, D. S. (2007). Depolarization in ice crystals and its effect on radar polarimetric measurements. *Journal of Atmospheric and Oceanic Technology*, *24*, 1256–1267.

Ryzhkov, A. V., & Zrnić, D. S. (2019). *Radar polarimetry for weather observations* (1st ed.). Springer.486.

Segall, J. H., French, M. M., Kingfield, D. M., Loeffler, S. D., & Kumjian, M. R. (2022). Storm-scale polarimetric radar signatures associated with tornado dissipation in supercells. *Weather and Forecasting*, *37*(1), 3–21. https://doi.org/10.1175/WAF-D-21-0067.1

Snyder, J. C., Ryzhkov, A. V., Kumjian, M. R., Khain, A., & Picca, J. C. (2015). A ZDR column detection algorithm to examine convective storm updrafts. *Weather and Forecasting*, *30*(6), 1819–1844. https://doi.org/10.1175/WAF-D-15-0068.1

Stalker, J. R., & Knupp, K. R. (2003). Cell merger potential in multicell thunderstorms of weakly sheared environments: Cell separation distance versus planetary boundary layer depth. *Monthly Weather Review*, *131*(8), 1678–1695. https://doi.org/10.1175/2556.1

TAHOPE. (2022). Taiwan-area heavy rain observation and prediction experiment. Retrieved from https://rain.as.ntu.edu.tw/TAHOPE/TAHOPE-home.html

Takahashi, T. (1978). Riming e–lectrification as a charge generation mechanism in thunderstorms. *Journal of the Atmospheric Sciences*, *35*, 1536–1548.

Tam, F. I.-H., Yang, M.-J., & Lee, W.-C. (2022). Polarimetric size sorting signatures in the convective regions of mesoscale convective systems in PECAN: Implications on kinematics, thermodynamics, and precipitation pathways. *Journal of Geophysical Research: Atmospheres*, *127*(10), e2021JD035822. https://doi.org/10.1029/2021JD035822

Tao, W.-K., & Simpson, J. (1989). A further study of cumulus interactions and mergers: Three-dimensional simulations with trajectory analyses. *Journal of the Atmospheric Sciences*, *46*(19), 2974–3004. https://doi.org/10.1175/1520-0469(1989)046<2974:afsoci>2.0.co;2

tobac Community, Brunner, K., Freeman, S. W., Jones, W. K., Kukulies, J., Senf, F., et al. (2023). Tobac—Tracking and object-based analysis of clouds [Software]. *Zenodo*. https://doi.org/10.5281/zenodo.8164675

T-PARCII. (2022). Tropical cyclones-pacific Asian research campaign for improvement of intensity estimations/forecasts. Retrieved from http://rain.hyarc.nagoya-u.ac.jp/~tsuboki/kibanS2/index_kibanS_eng.html

Tuttle, J. D., Bringi, V. N., Orville, H. D., & Kopp, F. J. (1989). Multiparameter radar study of a microburst: Comparison with model results. *Journal of the Atmospheric Sciences*, *46*(5), 601–620. https://doi.org/10.1175/1520-0469(1989)046<0601:mrsoam>2.0.co;2

Van Den Broeke, M. S. (2017). Polarimetric radar metrics related to tornado life cycles and intensity in supercell storms. *Monthly Weather Review*, *145*(9), 3671–3686. https://doi.org/10.1175/MWR-D-16-0453.1

Van Den Broeke, M. S. (2020). A preliminary polarimetric radar comparison of pretornadic and nontornadic supercell storms. *Monthly Weather Review*, *148*(4), 1567–1584. https://doi.org/10.1175/MWR-D-19-0296.1

Vivekanandan, J., Ellis, S. M., Oye, R., Zrnic, D. S., Ryzhkov, A. V., & Straka, J. (1999). Cloud microphysics retrieval using S-band dual-polarization radar measurements. *Bulletin America Meteorology Social*, *80*(3), 381–388. https://doi.org/10.1175/1520-0477(1999)080<0381:cmrusb>2.0.co;2

Westcott, N. (1984). A historical perspective on cloud mergers. *Bulletin America Meteorology Social*, *65*(3), 219–226. https://doi.org/10.1175/1520-0477(1984)065<0219:ahpocm>2.0.co;2

Wilson, M. B., & Van Den Broeke, M. S. (2021). Using the supercell polarimetric observation research kit (SPORK) to examine a large sample of pretornadic and nontornadic supercells. *Electronic Journal of Severe Storms Meteorology*, *17*(2), 1–38. https://doi.org/10.55599/ejssm.v17i2.85

Wu, Y.-J., Liou, Y.-C., Liou, Y.-C., Tai, S.-L., Chang, S.-F., & Sun, J. (2021). Precipitation processes of a thunderstorm occurred on 19 August 2014 in northern Taiwan documented by using a high resolution 4DVar data assimilation system. *Journal of the Meteorological Society of Japan*, *99*, 1023–1044. https://doi.org/10.2151/jmsj.2021-049

Xu, W., Zipser, E. J., Chen, Y., Liu, C., Liou, Y., Lee, W., & Jou, B. J.-D. (2012). An orography-associated extreme rainfall event during TiMREX: Initiation, storm evolution, and maintenance. *Monthly Weather Review*, *140*(8), 2555–2574. https://doi.org/10.1175/MWR-D-11-00208.1

Yang, S., Chang, Y., Cheng, H., Lin, K., Tsai, Y., Hong, J., & Li, Y. (2024). Improving afternoon thunderstorm prediction over complex terrain with the assimilation of dense ground-based observations: Four cases in the Taipei basin. *Weather and Forecasting*, *39*(3), 541–561. https://doi.org/10.1175/WAF-D-23-0149.1

Yu, S., Luo, Y., Wu, C., Zheng, D., Liu, X., & Xu, W. (2022). Convective and microphysical characteristics of extreme precipitation revealed by multisource observations over the pearl river Delta at monsoon Coast. *Geophysical Research Letters*, *49*(2), e2021GL097043. https://doi.org/10.1029/2021GL097043

Yuter, S. E., & Houze, R. A., Jr. (1995). Three-dimensional kinematic and microphysical evolution of Florida cumulonimbus. Part II: Frequency distributions of vertical velocity, reflectivity, and differential reflectivity. *Monthly Weather Review*, *123*(7), 1941–1963. https://doi.org/10.1175/1520-0493(1995)123<1941:tdkame>2.0.co;2